

Detailed observations of a naturally occurring shear instability

Harvey E. Seim and Michael C. Gregg

Applied Physics Laboratory and School of Oceanography, College of Ocean and Fishery Sciences, University of Washington, Seattle

Abstract. Simultaneous profiles of microstructure, horizontal velocity, and acoustic backscatter allow one of the most complete descriptions of a naturally occurring shear instability to date. Shear increased rapidly after passing through a lateral constriction which formed a hydraulic control. A kilometer-long set of 20-m-tall billows grew on a middepth density interface where the Richardson number fell below 0.25. The velocity interface thickened steadily after the billows formed, consistent with rapid momentum mixing across a shear layer with a Reynolds number of 3×10^6 . The billows generated large density overturns and dissipation rates greater than $10^{-5} \text{ W kg}^{-1}$, even within the first large overturn, indicating that these structures were fully turbulent early in their development. As the billows grew, a well-mixed layer developed at the interface and survived as an actively turbulent layer for up to 6 buoyancy periods, 3 times longer than in laboratory studies at low Reynolds number. Variations in the mean density of the billows lead us to infer that the vertical offset of the velocity and density interfaces varied with time where the billows first formed. With data from the large overturns within the shear layer, we find $\epsilon/\nu N^2 \approx 3 \times 10^4$, an average root-mean-square overturn scale (L_{rms}) of 2.6 m, and a buoyancy scale (L_b) of 2.7 m. Despite having sampled the billows at varying stages of their evolution, we find no indication that the ratio L_{rms}/L_b is ever significantly different than 1 for this shear instability.

1. Introduction

While steaming with the current along a deep tidal channel, we had the good fortune to sample a kilometer-long set of large billows (Plate 1). As the billows faded on the echo sounder, we turned the ship around to run upstream back through them. Because of the increasing tidal currents and problems retrieving our microstructure profiler, we fell back and then repositioned several times. But the current swept the billows downstream by us, allowing us to collect a second set of measurements.

This paper is a detailed presentation of our fortuitous encounter. Our simultaneous measurements of microstructure, acoustic backscatter, and horizontal currents provide a unique realization of energetic, naturally occurring billows. The turbulent behavior of these large instabilities is qualitatively different than their low Reynolds number laboratory counterparts; specifically, the billows are strongly dissipative from very early in their evolution and remain actively turbulent for up to 6 buoyancy periods, 3 times longer than found in laboratory studies [Thorpe, 1973; Koop and Browand, 1979].

Most intriguing, however, is the change in properties along the kilometer-long set of billows that must result

from changes in conditions where the billows first form. The mean density of individual billows varies within the set; we propose that this results from changes in vertical offset of the velocity and density interfaces. The longitudinal density structure we observe has important implications for the final state of the patch of mixed fluid produced by the instability. The dissipation rate within the billows varies with billow density, suggesting that the interface offset significantly affects the intensity of turbulence.

Section 2 describes our instrumentation and then the setting and spatial organization of the sampling. We give an overview of the data in section 3, including a simple model of the event that is consistent with the observations. Section 4 addresses the composition of mixed fluid produced when the shear layer becomes turbulent and how the outer scales and energy-containing scales of the mixing layer vary. We summarize our results and discuss the implications in section 5.

2. Background

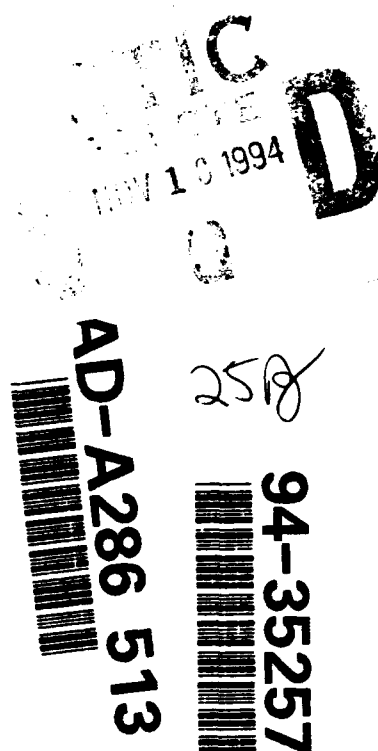
2.1. Instrumentation

Profiles of velocity and acoustic backscatter were collected continuously from the R/V *Miller*, a 15-m utility boat. A 150-kHz RD Instruments acoustic Doppler current profiler (ADCP) monitored the currents; BioSonics 120-kHz and 200-kHz narrow beam echo sounders im-

Copyright 1994 by the American Geophysical Union.

Paper number 94JC00168.
0148-0227/94/94JC-00168\$05.00

94 11 15 069



**Best
Available
Copy**

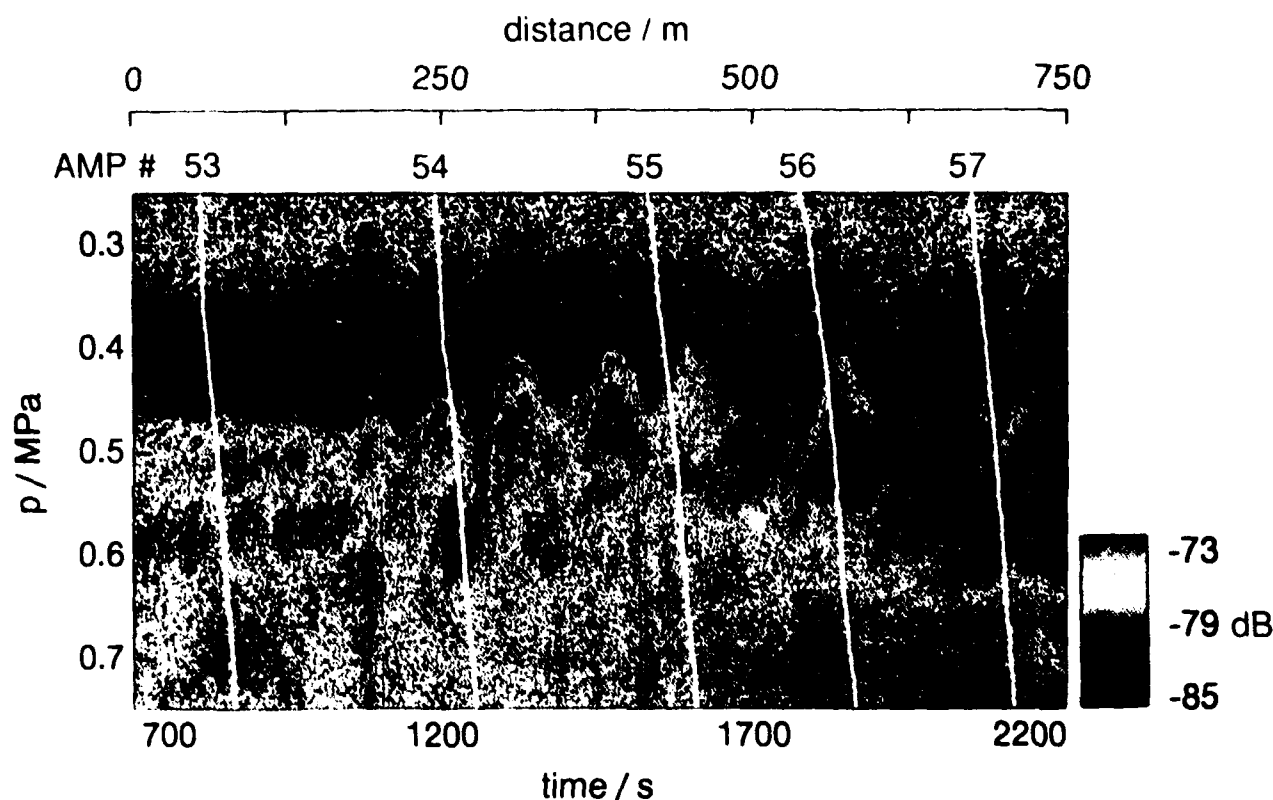


Plate 1. Acoustic backscatter image of the billows, overlaid with profiler trajectories (white lines), which run parallel to the sidelobe returns from the advanced microstructure profiler (AMP) (faint red lines). The vertical exaggeration is 5:1; pixel size is 0.125 m in the vertical and every second horizontally. AMP numbering gives the last two digits of drop numbers referred to in the text. Red corresponds to stronger backscatter, the scale being volume scattering strength in decibels per 1 μPa at 1 m. The distance scale is of ship motion relative to 0.5 MPa (50 m). The billows fade with time as they occur in decreasing stratification.

aged backscatter intensity. The free-falling, loosely tethered advanced microstructure profiler (AMP) measured vertical profiles of temperature, conductivity, centimeter-scale vertical shear of horizontal currents, and centimeter-scale vertical temperature gradients every 200–400 m along the ship track.

These three instrument systems provide distinctly different views of the shear instability. An invaluable unaliased two-dimensional picture of the water column is obtained by the echo sounders, without which we could not identify the billows. The ADCP measures the average change in the velocity field, although the averaging time is short enough that the large coherent structures contribute to short-term variations in the velocity estimates. On the other hand, the AMP collects a profile of point measurements (i.e., a small volume sample collected in a fraction of a second) relatively quickly. At 0.65 m s^{-1} , the profiler crosses a 20-m billow in about 30 s, a fifteenth of the average buoyancy period across the first large billow ($N \approx 0.014$). AMP profiles thus strongly reflect the phase of the coherent structures they sample; we examine the turbulence within the large-scale structures with these data. This variety of perspectives is advantageous, except when we form

variables by combining fields from different instrument systems; owing to the difference in averaging times, these variables are quite “noisy,” leading to a problem akin to salinity spiking. In particular, the Richardson number is formed from the AMP and ADCP data and appears quite noisy.

There is some uncertainty as to the exact ship trajectory over ground, because our navigation data are poor. Triangulation from radar ranges collected as the AMP drops began provides navigational fixes accurate to about 50 m. We interpolate between known positions for all AMP drops lacking fixes.

The ADCP data are averaged for 2 min, producing ensembles of about 240 pings. The averages have rms uncertainties of less than 2 cm s^{-1} . The vertical resolution of the ADCP is determined by the 4-m bins and 8 m pulse length, which approximate a Bartlett filter having a 3-dB point at 12 m. The vertical shear of the horizontal currents is formed by first-differencing the 4-m data; $S_{12}^2 \equiv (\Delta u / \Delta z)^2 + (\Delta v / \Delta z)^2$, where u and v are east and north velocity components, respectively, and Δz is 4 m. The subscript denotes resolution of scales larger than 12 m. Unfortunately, we are unable to form absolute velocities directly from the

ADCP data because bottom-tracking was not working. A problem with the compass installation on the *Miller* renders the measurements unreliable during large changes in direction and noisy at other times; we later note when this is a problem. We use a one-dimensional linked-channel tidal model to predict the absolute current speed [Lavelle *et al.*, 1988]. Details of the procedure are given in Appendix A.

The AMP was dropped from the stern of the *Miller* while under way, fell at $0.6\text{--}0.7\text{ m s}^{-1}$ to within roughly 10 m of the bottom, and was retrieved using the tether. Standard processing of the hydrographic data produces profiles with 0.1-m vertical resolution. Assuming isotropy, we form the dissipation rate of turbulent kinetic energy (ϵ) from the small-scale shear, and the dissipation rate of temperature variance (χ) from the vertical temperature gradient over 0.5-m segments as

$$\epsilon = 7.5\nu \int_{k_0}^{k_c} (2\pi k)^2 \Phi_\nu(k) dk \quad [\text{W kg}^{-1}], \quad (1a)$$

$$\chi = 6\kappa_T \int_{k_0}^{k_c} (2\pi k)^2 \Phi_T(k) dk \quad [\text{K}^2 \text{ s}^{-1}] \quad (1b)$$

where Φ_ν and Φ_T are the velocity and temperature spectra, respectively; ν is the kinematic viscosity; and k_0 and k_c are the lower and upper bounds of the integration, not necessarily the same for the two integrals. See Peters *et al.* [1988] and Wesson and Gregg [1994] for details. These authors estimate that absolute errors of ensemble averages are roughly a factor of 2. Appendix B is a brief discussion of dissipation rate errors.

Within the mixing event, much of the water column is statically unstable. To estimate the scale of overturns, we reorder the density profiles to be monotonically increasing, a procedure first proposed by Thorpe [1977]. By comparing the observed and reordered profiles, we form profiles of displacement (L_t), that is, the distance a parcel is moved within a profile to form a statically stable water column. To minimize false overturns resulting from salinity spiking, we sort both temperature and density and choose the sort that minimizes L_t . An overturn, h_{ov} , is the distance over which the running sum of the displacements is nonzero, $\sum L_t \neq 0$. Many of the parameters used in this article are defined as

L_t	displacement distance;
h_{ov}	overturn height (distance over which $\sum L_t \neq 0$);
$Re \equiv \Delta u h / \nu$	layer Reynolds number;
$Re_b \equiv \epsilon / \nu N^2$	buoyancy Reynolds number;
$Ri_b \equiv \Delta \rho g h / \rho (\Delta U)^2$	bulk Richardson number;
$h \equiv \Delta U / (\partial u / \partial z)_{max} $	vorticity thickness;
$L_\epsilon, \bar{\epsilon}$	thickness of elevated ϵ layer, mean ϵ over L_ϵ ;
$\epsilon_{ov}, \chi_{ov}, \rho_{ov}$	mean overturn properties;
$L_{rms} \equiv (\overline{L_t^2})^{1/2}$	root-mean-square displacement;

$$L_b \equiv (\epsilon / N^3)^{1/2} \quad \text{buoyancy (or Ozmidov) scale.}$$

Profiles of N^2 are formed from the reordered density (ρ) profiles, ensuring positive values of N^2 . We regard these estimates to be most representative of the buoyancy forces against which the turbulence acts. Without a subscript, N^2 is formed by differencing the density over 1 m, while N_{12}^2 denotes estimates formed after Bartlett filtering the density profiles to the same vertical scales as the ADCP data before differencing over 4 m. Estimates of the gradient Richardson number, $Ri_{12} \equiv N_{12}^2 / S_{12}^2$, are thus formed from variables with similar bandwidths.

Narrow beam echo sounders were used, having a 12-m^2 footprint (circle of radius 2 m) at 50-m depth, much smaller than the 50- to 100-m scale of the billows. Profiles were collected every second and digitized every 1/8 m. The acoustic system is calibrated, allowing us to convert images to volume scattering strength (VSS) using a sonar equation. In a separate study we compare the measured VSS with estimates of backscatter from the small-scale temperature variance measured by AMP (H. E. Seim *et al.*, manuscript submitted to the *Journal of Atmospheric and Oceanic Technology*, 1993) (hereinafter referred to as Seim *et al.*, 1993). The estimated VSS closely matches the measured VSS at the level of the billows, where the mean temperature gradient is largest, but elsewhere they are uncorrelated. We use this finding to justify interpreting the upper reflective horizon at this depth as an unaliased image of the temperature interface (Plate 1).

In order to do the backscatter/microstructure correlation study, it was necessary to estimate the position of AMP on the echo sounder image. Our technique amounts to spatially registering the AMP profile on the backscatter image (Seim *et al.*, 1993), as shown in Plate 1. We calibrate the model with the apparent echo from AMP in a transducer sidelobe for drops 5855-5858, which appear as faint red lines paralleling the model trajectories in Plate 1. (Only the last two digits of the AMP drop numbers are given on the plates and some figures.) We estimate that calculated trajectories are within ± 15 s of the true trajectory (see Seim *et al.* (1993) for details).

The acoustic images are collected while moving and thus represent changes in both space and time; they cannot be considered a "snapshot" of the spatial structure nor a time series of the evolution. The ship's motion distorts the horizontal scales by Doppler shifting; observed features of length L have a true wavelength of

$$\lambda = L(1 - U/U_{ship}) \quad (2)$$

where the flow velocity is U . Owing to shear in the water column, the Doppler shift varies with depth, further distorting the shape of features.

2.2. Setting

The data were collected in Admiralty Inlet, a 30-km-long tidal channel connecting Puget Sound and the Strait of Juan de Fuca (Figure 1). The latter leads to the open ocean. Puget Sound receives a considerable amount of runoff which drives a baroclinic exchange flow across Admiralty Inlet and makes it salt-stratified. A shear layer typically exists between the inflowing saline bottom layer and outflowing surface layer, providing a natural laboratory in which to study shear instability. The flow is complicated by the 2- to 4-m mixed (both diurnal and semidiurnal) tides of the northwest coast of North America, which in combination with the exchange flow gives rise to a time-varying shear flow.

Our samples were collected off Bush Point, a lateral constriction just seaward of the mouth of Hood Canal.

A series of sections was collected off Bush Point during and after an extended high tide. During most of these sections, wavelike and cat's-eye-like patterns in the water column appeared on the echo sounder. We here concentrate on the sections with the most extensive microstructure sampling and for which we have some navigation data.

The underlying cause of instability at this location appears to be linked to internal hydraulics. Bush Point forms a pronounced constriction that can act as a hydraulic control [e.g., *Armi, 1986*]. The influence of the topography on the ebbing flow is apparent in a sectionally averaged tidal transport model [*Lavelle et al., 1988*] that predicts a nearly twofold increase in current speed as the flow passes by Bush Point. Because of the oscillatory tidal flow, however, the control is not always active. For a two-layered flow, criticality is determined by the composite Froude number,

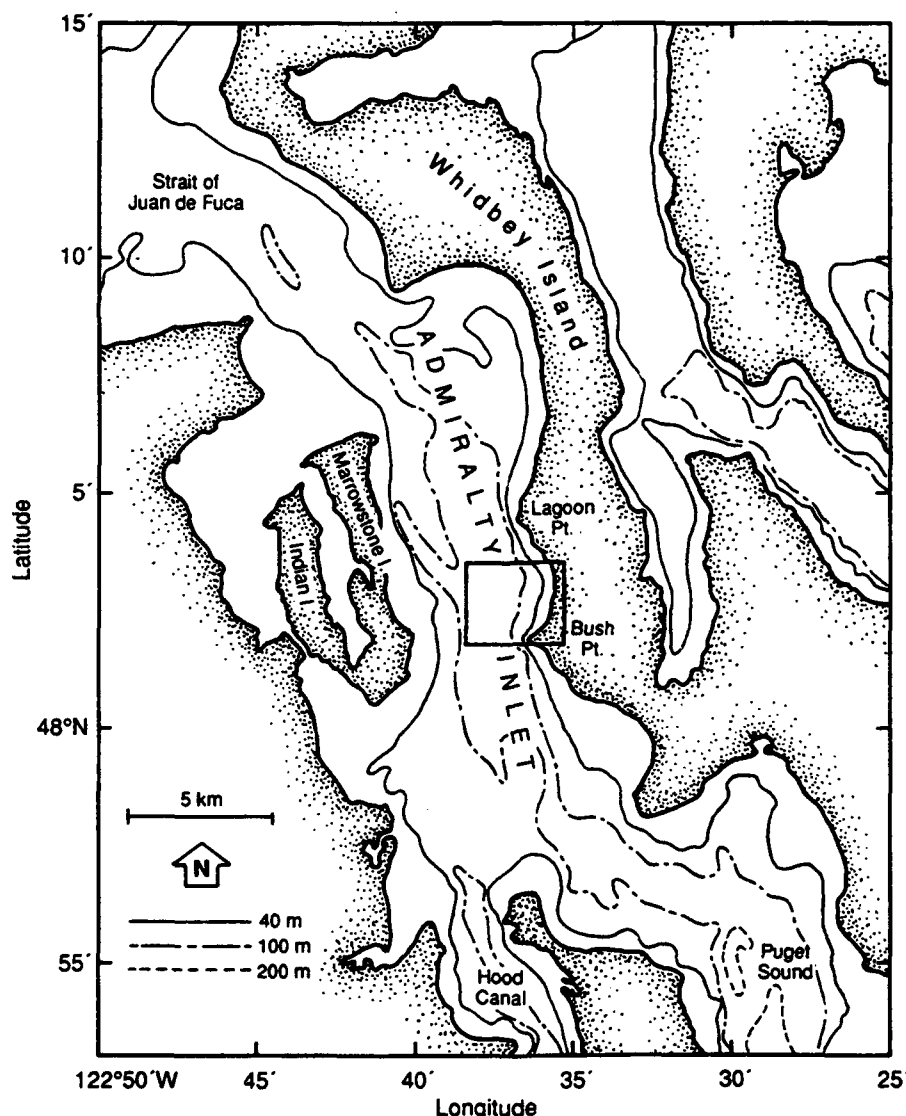


Figure 1. Location map and bathymetry of Admiralty Inlet. The box marks the study area. Note that Bush Point and Marrowstone Island constrict northward (ebbing) flow, making this section a hydraulic control when the density field is favorable (see text).

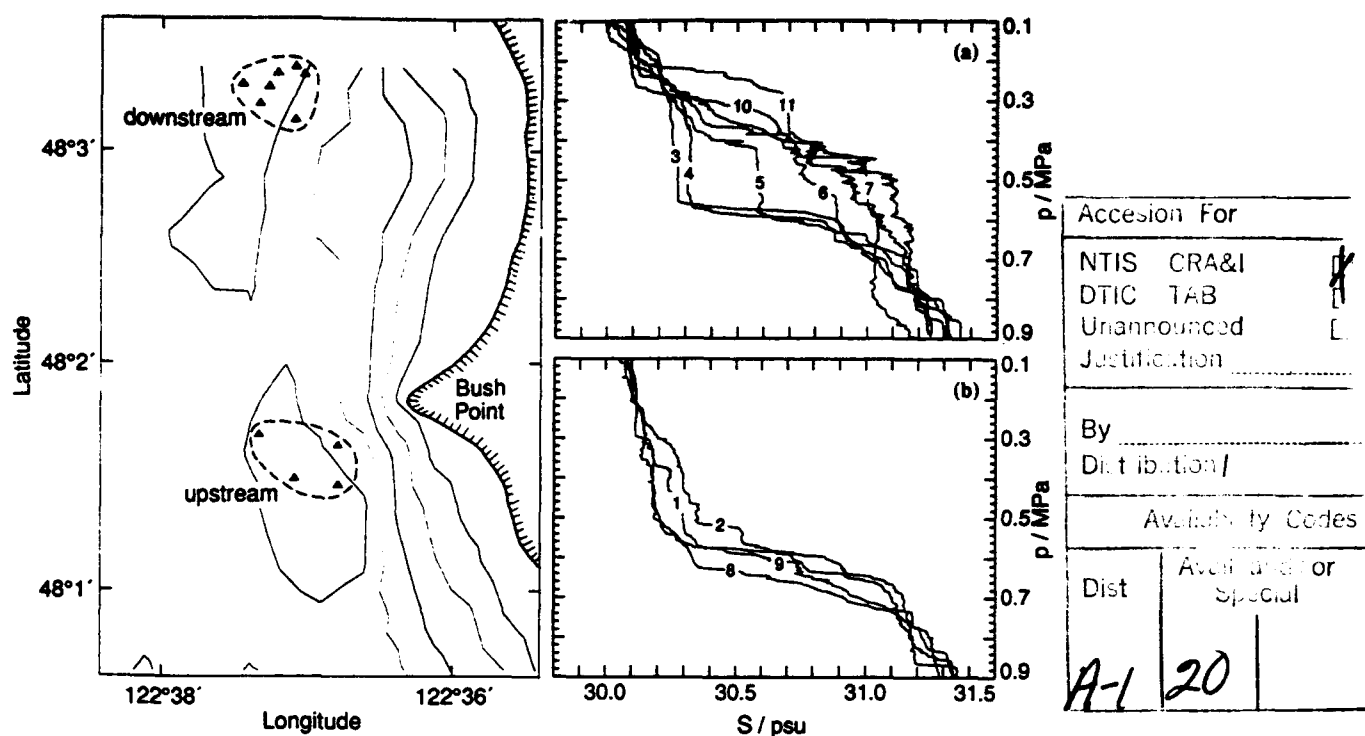


Figure 2. Salinity profiles (a) downstream and (b) upstream of Bush Point. Numbering shows the order in which the profiles were collected. The persistent interface at 0.6 MPa upstream and large changes in interface height downstream are consistent with critical flow conditions at Bush Point during the sampling period.

$$G^2 \equiv \frac{U_1^2}{g'h_1} + \frac{U_2^2}{g'h_2} \quad (3)$$

with U_n and h_n the speed and thickness of the layers, respectively, and $g' \equiv g\Delta\rho/\rho$ the reduced gravity. We observed a roughly two-layered flow, the surface layer being 1 kg m^{-3} lighter and flowing 0.5 m s^{-1} faster than the lower layer. At high water, when there is no net flow, there is an exchange flow ($U_1 = -U_2$ and $h_1 = h_2 = 50 \text{ m}$). Then $G^2 = 0.25$, the flow is subcritical, and the constriction off Bush Point does not act as a control. As the flow begins to ebb, the layer velocities change and G^2 begins to increase. We find that the flow will be critical ($G^2 = 1$) at Bush Point for mean flow speeds $((U_1 + U_2)/2)$ in excess of 0.43 m s^{-1} . During our observations, the flow speed increased from below this value to well above it, suggesting we observed the transition through criticality and the establishment of hydraulic control.

Changes in height of the density interface downstream of Bush Point, but not upstream, confirm this interpretation. In a set of profiles collected upstream of Bush Point, before and after the billows samples, the interface is centered around 0.6 MPa (Figure 2b). In profiles collected downstream of Bush Point the interface is initially at 0.6 MPa (Figure 2a, profile 3), indicating subcritical conditions throughout the region. The interface downstream then rises from 0.6 MPa to 0.3 MPa (profiles 3–7) as control is established. The bil-

lows were observed during the transition. Samples after the billows (profiles 8–11) find the interface still raised downstream of Bush Point but unchanged upstream, confirming hydraulic control of the internal flow.

During the transition from subcritical to supercritical flow, the velocity and density interfaces are separated. The density interface rises first, followed by the velocity interface. Because shear instability occurs at the level of maximum shear, not maximum stratification, the difference in vertical location of the two interfaces significantly impacts the composition of the billows formed.

Because billows have roughly zero phase velocity relative to the mean flow [Ho and Huerre, 1984], an instability within a mean flow evolves downstream of the generation site because it cannot propagate upstream. If the phase speed of the forcing that produces $Ri < 0.25$ moves downstream, the event will appear as a transient at a fixed spatial coordinate. In the x - z plane, the billows will all be at a similar stage of development, their growth being obvious only by examining changes in time (Figure 3a). If, however, the forcing is topographically fixed, the instability grows only in the downstream direction. In this case, x - z plane realizations from different times will all be similar (Figure 3b).

Though a hydraulic control should generate a spatially growing instability, the flow acceleration due to the tides makes the flow unsteady. Having never re-sampled the Bush Point cross section, we cannot say whether $Ri < 0.25$ was maintained there for very long.

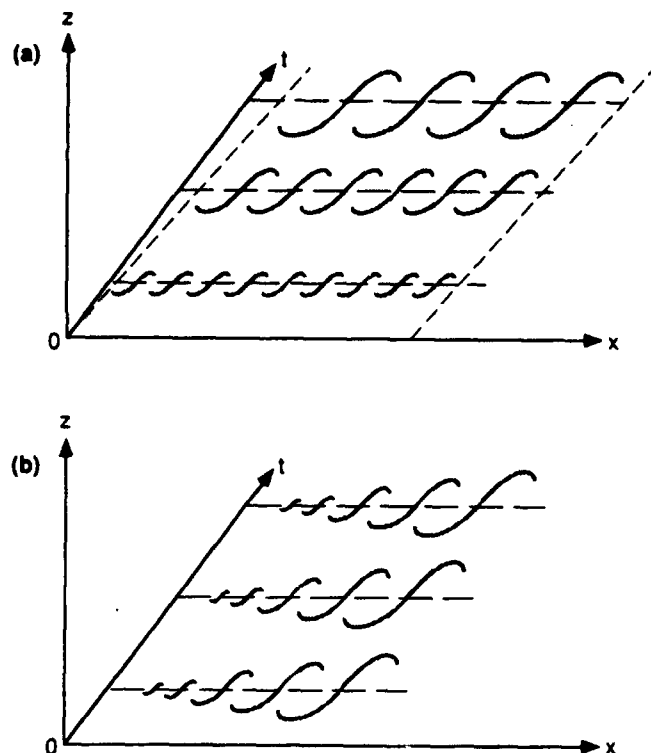


Figure 3. Sketch of two types of spatially growing instabilities. The plane of the page is the x - z plane, with time increasing into the page. (a) Transient evolution; billows at same phase of development at all x , evolving only with time. Dashed lines mark position of the packet as it is advected downstream. (b) Spatially growing; billows at same phase of development for all time, evolving only with x .

We have insufficient information to specify the form of evolution of the instability. By following the billows at their advection speed, though, we can assess their evolution in time, regardless of the space-time development of the shear layer. Not knowing if the instability evolves spatially or temporally, the only way to unambiguously measure its growth or decay is in a frame of reference moving with the shear layer. We adopt this coordinate system when assessing evolution.

Spatially growing instabilities associated with constrictions were found by Geyer and Smith [1987] in the lower reaches of the Fraser River on ebb tide. Together these studies suggest that lateral constrictions can strongly influence vertical mixing in channelized, stratified flows.

2.3. Sampling Pattern

On March 26, 1988, soon after the end of an extended high tide (Figure 4a), a series of wavelike features was observed at middepth on the echo sounder as the vessel steamed northward, with the ebbing current, past Bush Point (Figure 5). The ship was in the east half of the channel and passed over a small rise late in the section, covering 3.4 km over ground (Figure 4b). We designate

the set of AMP profiles collected during this time as section A.

As the acoustic signature of the features faded, the vessel turned southward and steamed into the current. The *Miller* did not make headway and was carried north, downstream, while steaming into the current; the four profiles collected at this time form section A1. After repositioning about 500 m to the south, three profiles were collected while slipping northward, paralleling section A1; these we designate section B. Three more profiles were subsequently collected, called post-B (Figure 4b). Table 1 summarizes the drop numbers and times of each of the sections.

The ship trajectory relative to the billows is found by integrating the relative velocity between the ship and the water at 0.5 MPa, the depth at which the billows are centered (Figure 4c). We estimate the ship track during the few minutes between drops 5858 and 5859 when the *Miller* reversed direction owing to a problem with the compass at that time (marked with a dashed line on Figure 4c). Sections A1 and B apparently sample within a few hundred meters of the fluid in which the billows were found in section A. Section A1 samples roughly the same water mass at the north end of section A, while section B samples near the first billows seen in section A. The later drops (post-B) sample the same downstream area as the earlier sections (Figure 4b) but well after the billows observed in section A have advected downstream.

In summary, the *Miller* steamed 3.4 km downstream relative to the bottom with the current while collecting section A. She then turned into the current and tried to hold position, but fell off while profiling, forcing her to reposition. Relative to the flow at the depth of the billows, the *Miller* sampled a 1.8-km segment on section A, then turned into the current, such that the fluid sampled in section A was advected past the ship. It appears that sections A1 and B sample approximately the same fluid as in section A. We call the latter reference frame billows-following and the former geographic. They are surrogates for Lagrangian and Eulerian reference frames.

3. Observations

This overview presents the observations for each of the sections sequentially. After section A we offer an interpretation of what we sampled.

3.1. Section A

3.1.1. Before billows. As section A begins, the water column is continuously stratified, but by AMI 5852, two moderately stratified layers ($N \approx 0.005 - 0.015 \text{ rad s}^{-1}$) are separated by a high-gradient region ($N \approx 0.03 \text{ rad s}^{-1}$) (Figure 6). The mean densities of the two layers differ by 0.9 kg m^{-3} with about a 0.5 kg m^{-3} change across the high-gradient region

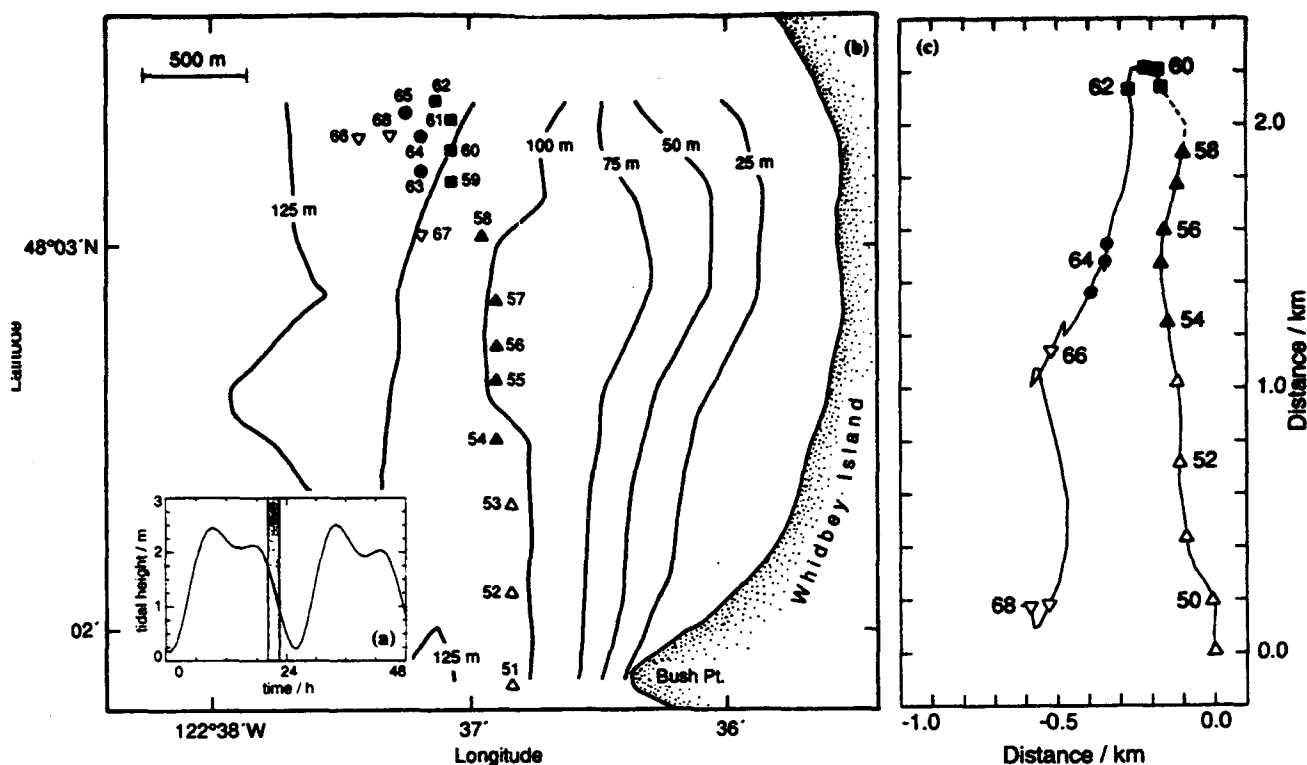


Figure 4. (a) The tides, with the measurement interval shaded. Sampling begins at the end of an extended high water and continues through maximum ebb. (b) Enlarged location map, showing the eastern half of the channel as outlined in Figure 1. Solid symbols mark drops which passed through billows or large overturns. Triangles mark drops from section A, squares mark section A1, circles mark section B, and inverted triangles mark post-B. (c) Progressive vector displacements of ship motion relative to 0.5 MPa, which presents the sampling pattern in a billows-following reference frame. Dashed line marks the estimated trajectory discussed in the text. Symbols are as in Figure 4b.

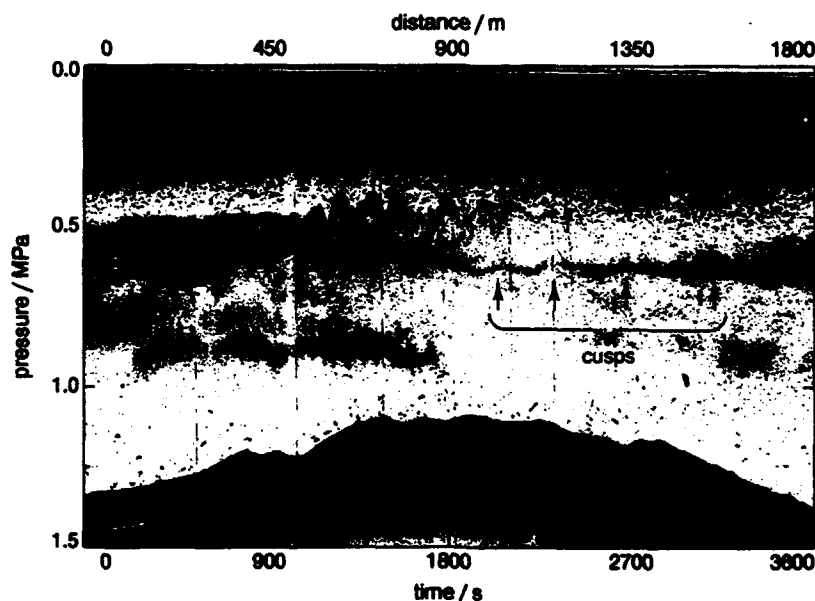


Figure 5. Uncorrected acoustic image of sections A-A1 showing the location of the billows relative to bathymetry. The dark region at the base of the image is the bottom. Note cusping of scattering layers above the billows and at 0.6 MPa for time greater than 1800 s. We interpret it as the result of circulation around the billows.

Table 1. Section Drops and Times on March 26, 1988

Section	AMP Drops	Times*
A	5849-5858	2008-2105
A1	5859-5862	2112-2130
B	5863-5865	2141-2155
post-B	5866-5868	2205-2232

*Times are in UTC.

AMP, advanced microstructure profiler.

The velocity field is also roughly two-layered, exhibiting weak shear in the two layers and larger shear across the high-density gradient. The velocity difference, ΔU , between the layers is about 0.45 m s^{-1} . Between drops 5849 and 5853, the gradient region between the two layers thins and rises from below 0.6 MPa to above 0.5 MPa, during which time N_{12}^2 doubles to $8 \times 10^{-4} \text{ s}^{-2}$ and S_{12}^2 triples to over $2 \times 10^{-3} \text{ s}^{-2}$. The echo sounder reveals a nearly horizontal scattering layer at the depth of the high N^2 region which also thins and rises (Plate 2).

The Reynolds number across the interface is very large, $Re \equiv \Delta U h / \nu = 3.5 \times 10^6$, where the vorticity thickness, $h \equiv |\Delta U / (\partial u / \partial z)_{\max}|$, is 11 m in AMP 5852 and $\nu = 1.4 \times 10^{-6} \text{ m}^2 \text{ s}^{-1}$. This value of initial Re is comparable to the Re of atmospheric billows observations and is 100 times larger than most numerical and laboratory experimental studies of stratified shear lay-

ers [Thorpe, 1987], with the notable exception of work on high-speed shear layers [e.g., Brown and Roshko 1974; Dimotakis, 1989].

In the lower portion of the high shear layer, $Ri_{12} < 0.25$ in drops 5852-5853 (Figures 6 and 7), owing to the maximum N_{12}^2 layer being thinner and offset upward from the layer of maximum shear. Setting $\Delta \rho = \Delta U = 0.5$, the bulk Richardson number $Ri_b \equiv \Delta \rho g h / \rho (\Delta U)^2$ rapidly decreases from 0.38 AMP 5850 to 0.21 in AMP 5852 as h changes from 20 m to 11 m. The high-gradient region therefore satisfies the necessary condition $Ri < 0.25$ [Miles, 1961] for instability. The first large-scale billows are obvious in AMP 5854, but smaller structures are visible before this, beginning at AMP 5853.

The increase in S_{12}^2 between profiles 5850 and 5853 appears to "trigger" the billows. The 10-m rise of the velocity and density interfaces while passing Bush Point implicates the constriction as the cause of the shear enhancement. A thinning interface implies $\partial w / \partial z < 0$. However, in the contraction (y downstream), $\partial u / \partial x$ is also negative, requiring a large downstream acceleration ($\partial v / \partial y > 0$) to satisfy continuity. Field acceleration may provide the necessary force.

The water column before the appearance of the billows is far from quiescent. At all depths ϵ seldom fall below $10^{-8} \text{ W kg}^{-1}$ and typically exceeds $10^{-6} \text{ W kg}^{-1}$ at several depths. The buoyancy Reynolds number $Re_b \equiv \epsilon / \nu N^2$, a commonly used measure of turbulent activity, typically exceeds 100 over much of the water

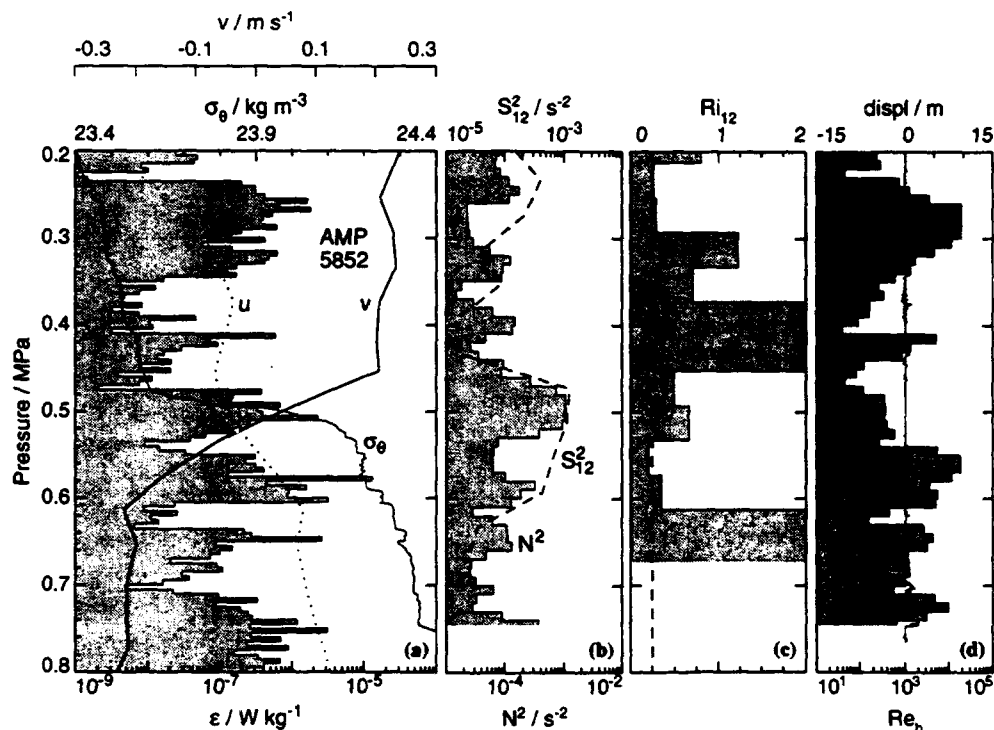


Figure 6. AMP 5852, collected prior to the appearance of the large billows: (a) density (σ_θ), 2-min averaged velocity (u, v), and ϵ ; (b) N^2 (shaded) and S_{12}^2 (dashed); (c) Ri_{12} , with the dashed line marking 0.25; and (d) Re_b and L_t . The σ_θ and N^2 profiles end at 0.77 MPa because of a clogged conductivity sensor below this depth.

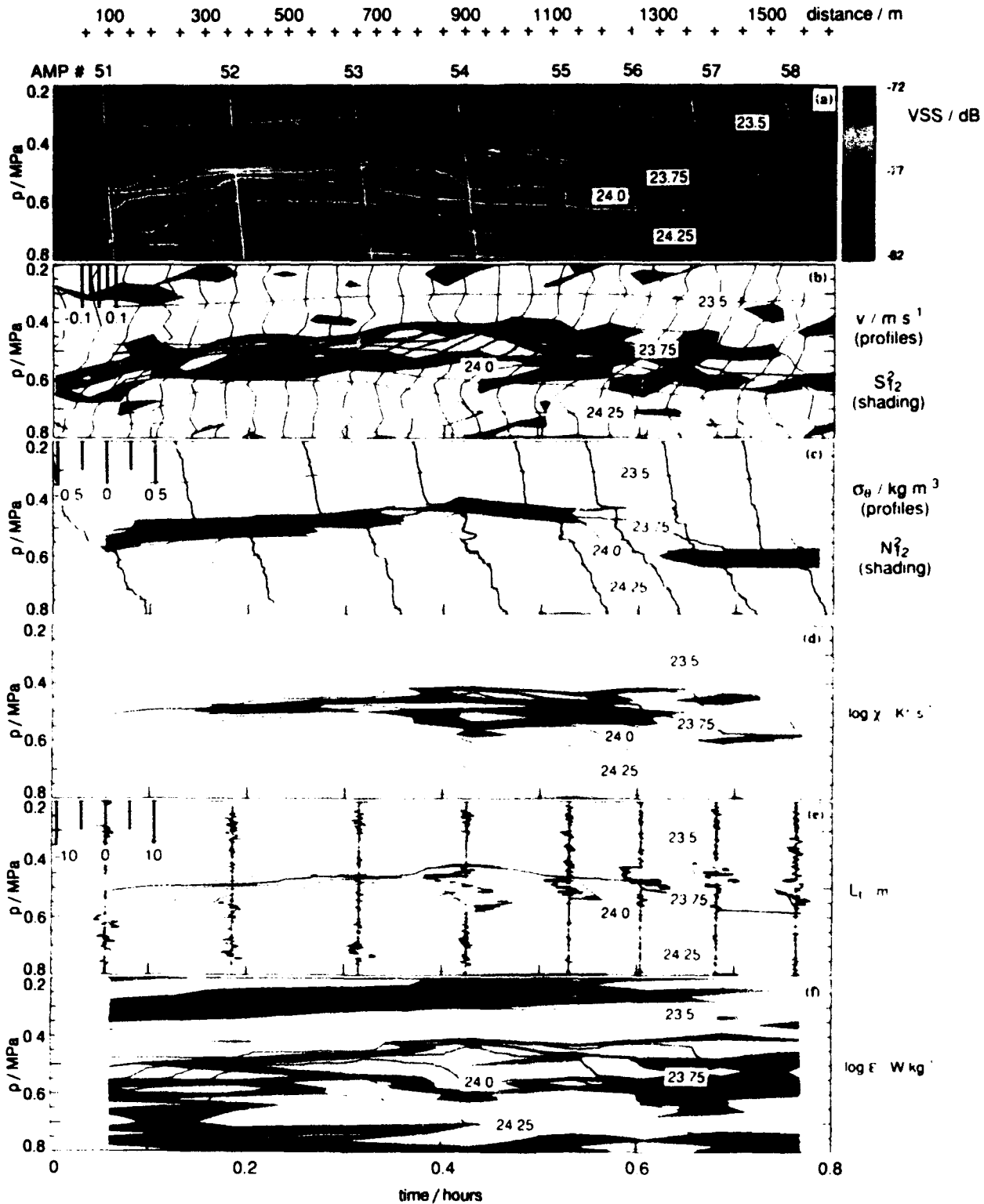


Plate 2. Summary of section A. All panels have in common the bottom axis and contours of density. Note that contours from AMP data are aliased and do not reflect horizontal features $< 300 \text{ m}$. (a) Acoustic image of the billows overlaid with AMP trajectories. (b) The 2-min averaged ADCP velocity profiles. Blue shading shows where $S_{12}^2 > 3 \times 10^{-4} \text{ s}^{-2}$, and yellow shading shows where $3 \times 10^{-4} < S_{12}^2 < 10^{-3} \text{ s}^{-2}$. (c) Density profiles from AMP; shading is for N_{12}^2 , using the same levels as for S_{12}^2 . (d) Contours of $\log \chi$. (e) Profiles of L_t . (f) Contours of $\log \epsilon$. In Plate 2d and 2f, values greater than -7 are shaded with a contour interval of 1.

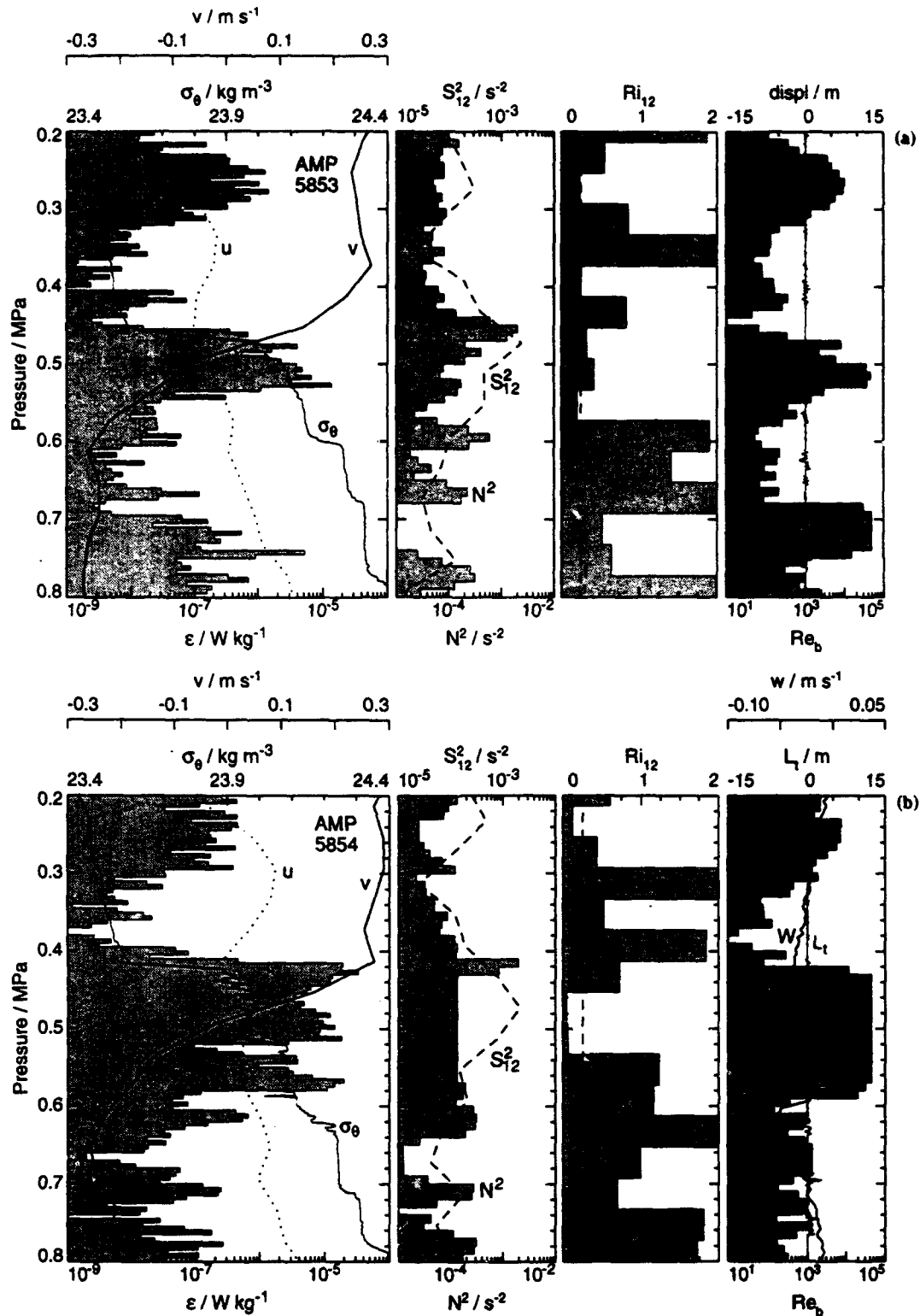


Figure 7. Profiles (a) as features appear below the interface (drop 5853) and (b) through first large billow (drop 5854). The various panels are described in Figure 6, except vertical velocity (w) is added to the right-hand panel of Figure 7b (see text).

column, well above the minimum value of 30 needed for the turbulence to support a negative buoyancy flux in grid-generated turbulence [Rohr *et al.*, 1988]. Where Re_b exceeds 200 the turbulence is isotropic at dissipation scales, and where $Re_b > 4 \times 10^4$, fully developed isotropic inertial subranges can be anticipated [Gargett

et al., 1984]. At the level where N^2 is largest, $Re_b < 10^3$ in drops 5850–5852, considerably less than peak values greater than 10^5 found outside the high-gradient region (Figure 6) but high enough to support active mixing. Displacement profiles indicate the high gradient region remains quite stable (Figure 6).

3.1.2. Billows. Beginning at AMP 5853, the mid-depth scattering layer develops wavelike features (Plate 2) which quickly grow, appearing to overturn as AMP 5854 is collected. We interpret the features as billows because of their location at a sheared density interface. The acoustic signatures of the billows fade as the vessel moves northward; by AMP 5858 they are no longer visible. As discussed below, the billows occur in progressively less stratified fluid to the north, resulting in rapidly decreasing values of χ (Plate 2), consistent with our contention that the backscatter at this depth results from scattering off refractive index microstructure. Mimicking where N^2 is largest, by AMP 5856 a scattering layer develops at 0.6 MPa which persists through the end of section A1, after the upper scattering layer fades away.

In the billows-following frame (Figure 4c) the average wavelength over the first four billows is 70 m. If the billow advection speed equals the mean shear layer velocity, as predicted by theory and observed in the laboratory, then Doppler shifts should be removed from this estimate of the wavelength. The peak-to-trough amplitude of the billow sampled by AMP 5854 is about 15 m on the echo sounder image, increasing to a maximum of 20 m in AMP 5855.

Beginning with AMP 5854, displacement profiles show a large overturning region (Plate 2c) which corresponds to the location of the billows on the echo sounder. The overturns are initially below the density interface (23.75 kg m^{-3}) but occur above it by the end of section A, as demonstrated by overlaying the density profiles for AMP 5854–5858 (Figure 8). Dissipation profiles show ϵ and χ enhanced over the same 5- to 20-m-thick sections

where billows appear on the echo sounder and the displacement profiles reveal large overturns (Plate 2). The billows are also apparent in profiles of χ . Even more dramatically than ϵ , χ becomes large only at the depth of the billows (Plate 2d).

The velocity interface spreads after drop 5854, causing S_{12}^2 to decrease (Plate 2b) and the vorticity thickness to increase from 11 m in AMP 5852 to 22 m in AMP 5858. The change in the velocity profiles is consistent with rapid momentum mixing at the interface beginning at drop 5854. It would be surprising if the decrease in shear (thickening of the shear layer) were due to the increasing channel width. Continuity suggests the divergence of the cross-stream flow would be balanced by thinning of the layer, $\partial u / \partial x = -\partial v / \partial y - \partial w / \partial z > 0$ or $\partial w / \partial z < 0$. We may actually underestimate the vorticity thickness downstream of Bush Point.

The acoustic images give no indication of vortex pairing, consistent with the large initial Ri as found by *Koop and Browand* [1979], although *Brown and Roshko* [1974] note pairings are difficult to identify in still shots (they use cinefilms to identify pairing events). The data from AMP 5854, however, strongly suggest the profiler passed through two billows (Figure 7b). The vertical velocity within the billows, estimated from perturbations in AMP's fall rate (see H. E. Seim and M. C. Gregg, manuscript in preparation, 1993) (hereinafter referred to as Seim and Gregg, 1993), shows two maxima and two minima, mimicking the displacement profiles. This is inconsistent with a single vortex; a near-vertical profile through a spanwise vortex possesses at most one significant maximum and minimum. The sense of motion is as expected, dense fluid rising and light fluid sinking. Interestingly, simulations by *Fritts* [1984] of pairing at a strong density interface produce a density field, and billow structure, similar to that measured in AMP 5854 (Figure 9).

To summarize, section A begins in a roughly two-layer flow. Passing Bush Point, the high-gradient regions of both the velocity and density fields thin and rise, greatly increasing the gradients between the two layers and leading to $Ri_{12} < 0.25$ in the lower half of the shear layer in AMP 5852 and 5853. The unaliased acoustic image demonstrates the interface is initially smooth along the flow. Coherent structures appear beneath the interface, where $Ri_{12} < 0.25$ at AMP 5853 and rapidly grow to 20-m billows by AMP 5855. AMP profiles through the billows reveal large-scale overturning of the density field within the billows and large dissipation rates. As we move north through the set of billows, density profiles show that the billows occur in progressively less dense fluid. This lighter fluid is also less stratified. Consequently, turbulence within the billows generates less χ to the north, causing the acoustic signature of the billows to fade out. Velocity profiles indicate that shear rapidly decreases and the vorticity thickness increases after the billows form. This is consistent with the extraction of energy from the mean shear by the shear instability and resulting turbulence.

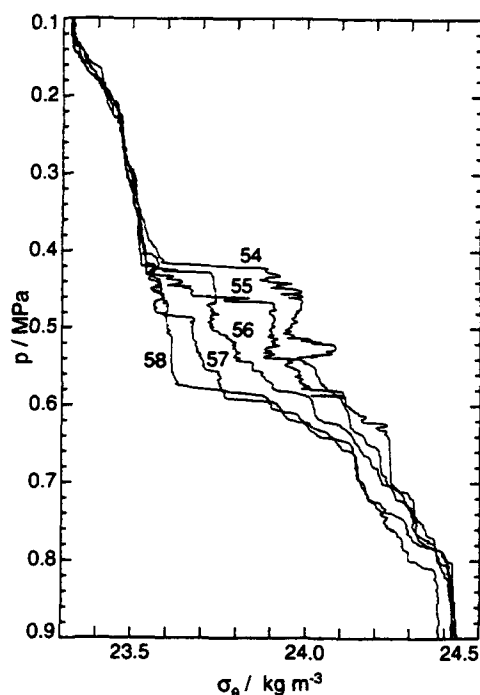


Figure 8. Overlaid density profiles for AMP 5854–5858, demonstrating the decrease in density of the billows to the north in the billows-following frame.

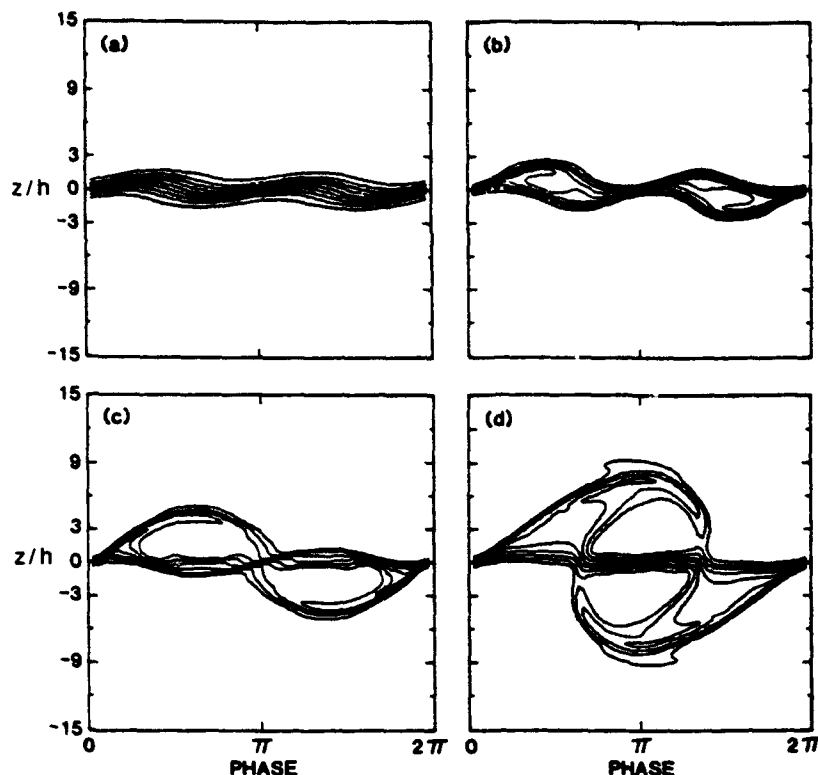


Figure 9. Contours of density field showing a pairing event at a strongly stratified, sheared interface from simulations by *Fritts* [1984]. The structure is similar to that seen in the acoustics, and a vertical profile through the paired billows in Figure 9d would closely resemble AMP 5854.

3.1.3. Interpretation. If the shear layer is spatially growing and statistically steady in time (in a geographic reference frame), the density of the billows would rapidly change as they move downstream. The billows would entrain large amounts of fluid only from the upper layer and would grow dramatically. Because they at best maintain their size after AMP 5855, this model of the evolution is not physically realistic. Apparently, conditions are not steady.

We now present a simple cartoon that explains the observed longitudinal density structure. The billows form as critical conditions are established at the constriction; it seems reasonable that the density structure of the billows is related to this time-dependent process. Figure 10a shows the two-layer, inviscid development of controlled flow, based on a model of a similar process over a sill [*Geyer*, 1990]. Initially, the flow is subcritical throughout, with the interface at height z_0 ; the interface smoothly shoals at the constriction (the upper layer is assumed to be active). As the tidal currents accelerate the flow to critical conditions at the constriction, a cusp forms that subsequently propagates downstream, raising the interface and establishing a growing regime of supercritical flow downstream of the control.

Now consider a position slightly downstream of the constriction (x_0) where a spatially growing shear instability originates. As critical conditions at the constriction are established, the interface at x_0 is depressed relative to its height at the control, causing it to be

centered beneath the velocity interface (Figure 10b, profile 1). As the cusp propagates through x_0 , the interface rises; we propose that this occurs more rapidly than the velocity field can respond, so the density interface is temporarily centered above the velocity interface (Figure 10b, profile 3). After the cusp has moved far downstream of x_0 , the two interfaces realign at a higher position in the water column, z_1 .

Figure 10c is a snapshot of the density field downstream of x_0 for the viscous case when billows form. At time 1, the density interface is beneath the velocity interface, and billows form above the density interface. At time 2, the density interface has risen to the shear maximum, and the billows now entrain equal amounts of fluid from both sides of the density interface. By time 3, the density interface is above the velocity interface, and the billows form beneath it. Fluid from time 1 is now far downstream of the origin (Figure 10c), fluid from successively later times being closer to the origin. The resulting density structure is in good agreement with our observations (Plate 2c) and resembles a smoothed version of Figure 10a at an intermediate stage of development.

Cusps on the scattering layer near the end of section A (Figure 5) likely result from billows centered above it at 0.5 MPa. This is consistent with our model that the density interface was centered beneath the shear layer when these billows first formed. When the velocity and density interfaces are of different thicknesses

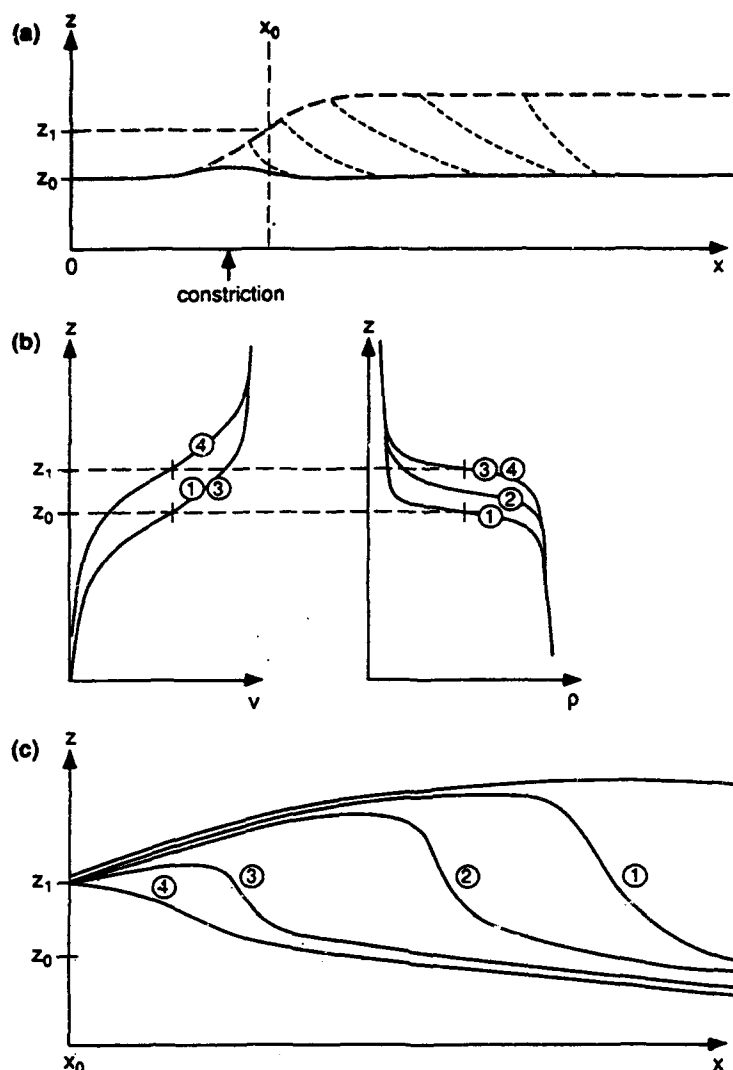


Figure 10. (a) Sketch of the development of hydraulic control at a constriction as the tidal current increases. Initially, the flow is subcritical (solid line), the interface rising only at the constriction. As critical conditions ($G^2 = 1$) occur at the constriction, a cusp forms, which subsequently moves downstream, establishing a growing region of supercritical flow. (b) Conditions at x_0 where the shear instability originates. The density interface moves from below the velocity interface as the cusp first forms (1), to centered at the same location (2), to slightly above (3). After the cusp is far downstream, both interfaces realign at a new position, z_1 (4). (c) The resulting density structure downstream of x_0 . Fluid from (1) is farthest downstream.

and offset a fixed amount, recent laboratory studies of shear instabilities find that billows form at the level of maximum shear, causing the density interface to cusp or $Ri \approx 0.25$ [Lawrence *et al.*, 1991]. As Ri is decreased, the cusps become more peaked and fluid is entrained across the interface into the spanwise vortices. We speculate that changing the offset between the interfaces will produce similar variations in the amount of fluid entrained by the billows.

3.2. Sections A1, B, and Post-B

The longitudinal density structure and large-scale overturning of the billows is also seen in the later profiles. However, because ship speed varies substantially,

the acoustic imagery is difficult to interpret, and billows are no longer obvious on the echo sounder. We omit these images, but note that cusps on the scattering layer at 0.6 MPa in section A1 (Figure 5) and the persistence of structured scattering layers at 0.4–0.5 MPa in section B suggest the continued presence of coherent structures at middepth.

In section A1, large overturns occur in weakly stratified fluid above the main density interface at 23.75 kg m^{-3} (Figure 11). Within the overturns, ϵ is comparable to values at the end of section A, but χ is small, rising above $10^{-7} \text{ K}^2 \text{ s}^{-1}$ only within the stratified fluid beneath the overturns, where ϵ is also elevated.

Section B samples water that was stratified in AMP 5856 and 5855 of section A (Figure 4c), but by AMP

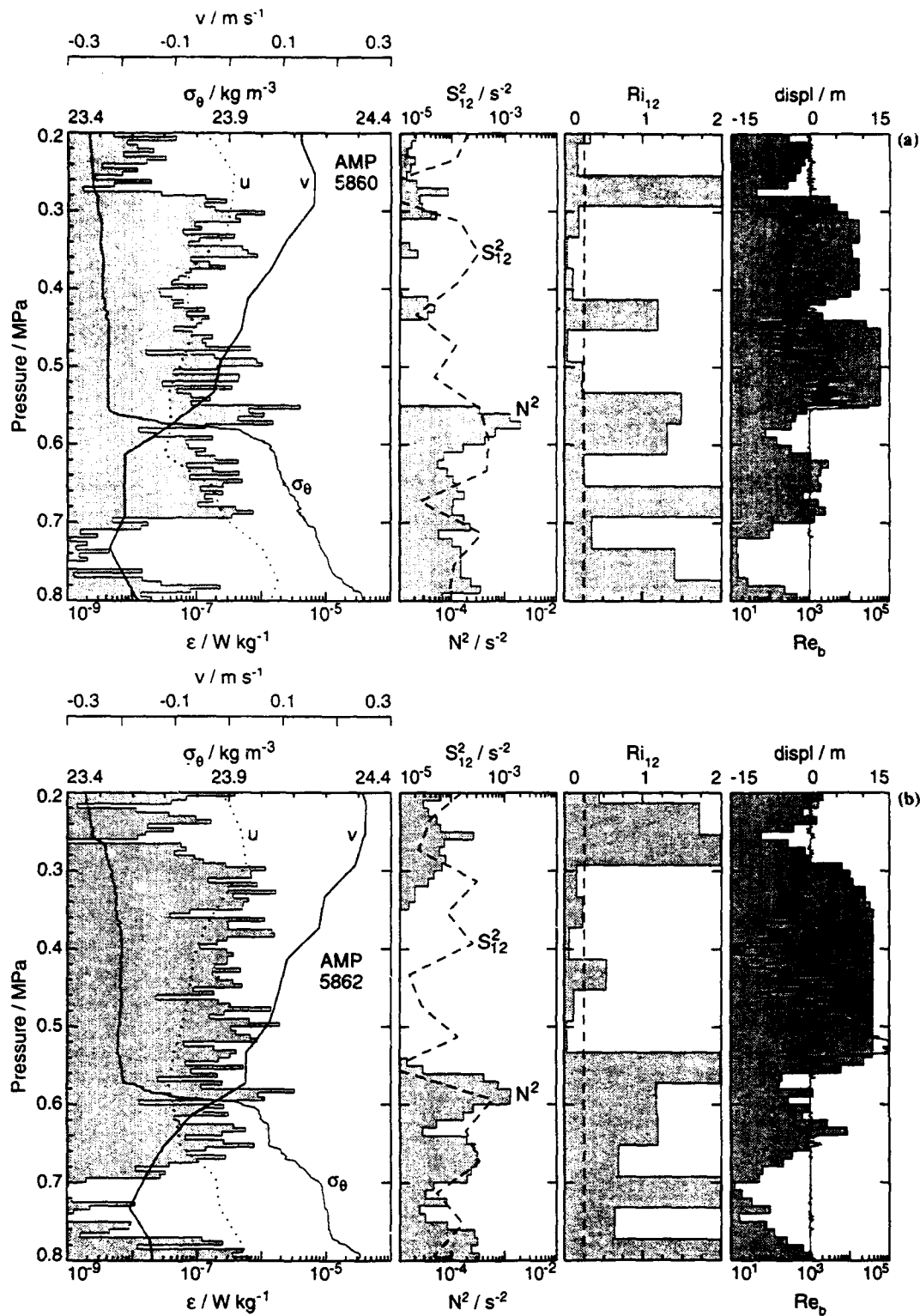


Figure 11. AMP 5860 and 5862 from section A1. Fields in each panel are as in Figure 4. Large overturns and ϵ occur in weakly stratified fluid above the main density interface; high ϵ persists through the interface in both drops.

5863 and 5864, section B contains an obvious 20-m-thick well-mixed layer whose density is roughly 0.2 kg m^{-3} greater than in section A1. The large overturn is centered near $\sigma_\theta = 23.75 \text{ kg m}^{-3}$ and is associated with elevated ϵ (Figure 12a). At the edges of the well-mixed layer, centered at 0.5 MPa, χ rises above $10^{-7} \text{ K}^2 \text{ s}^{-1}$.

Distinct from the rest of the profiles, in AMP 5865 the density field is stratified over much of the region of elevated ϵ , possibly the result of collapse of the billows, although ϵ still exceeds $10^{-6} \text{ W kg}^{-1}$.

Velocity profiles for both sections continue the trend of weakening shear seen in section A. Both S_{12}^2 and

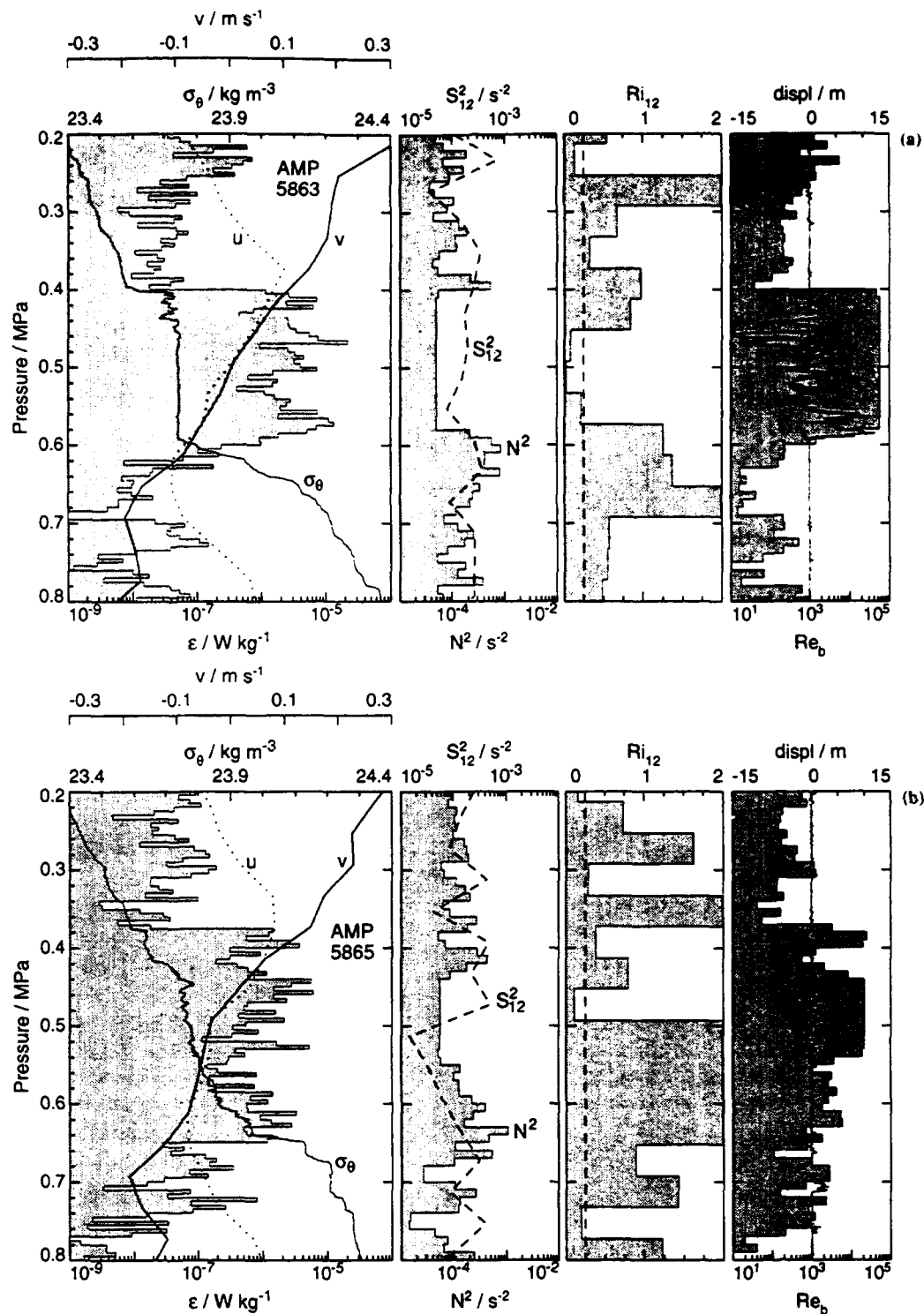


Figure 12. AMP 5863 and 5865 from section B. Fields in each panel are as in Figure 4. Large overturns are centered on the main density interface in AMP 5863. In AMP 5865 the density field is more stratified, but a pronounced ϵ layer extends over 28 m.

N_{12}^2 are reduced by at least an order of magnitude at 0.5 MPa relative to conditions before the billows (Figures 11 and 12). The Ri_b values for sections A1 (0.4–0.6) and B (0.2–0.5) are well in excess of 0.33, a value that *Thorpe* [1973] found to be the maximum achieved in his laboratory work and that *Geyer and Smith* [1987] observed to be the preferred value during ebb in the

Fraser River estuary. It may be that growth cessation exhibits some Re dependence, and shear layers with very large Re persist to slightly larger Ri .

The three additional profiles collected after section B demonstrate that velocity and density fields have changed considerably (Figure 13). Large shear is now concentrated above 0.4 MPa, and $Ri_{12} > 0.25$ (although

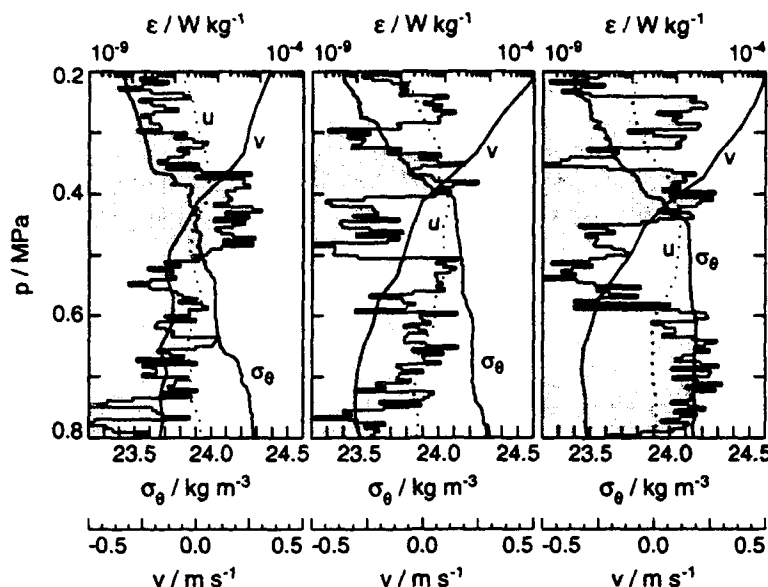


Figure 13. Profiles 5866–5868 collected after the mixing layer is no longer apparent.

not much) in this depth range for all three profiles. While there is a 10-m overturn between 0.4 and 0.5 MPa in AMP 5866, the other two profiles do not display any large overturns where ϵ is high in the shear layer. Conditions have changed enough that the middepth mixing layer no longer exists.

In summary, after section A the vessel turned into the current, roughly staying with the north end of the set of billows while collecting section A1. These profiles reveal large overturns centered above the density interface. Repositioning to a billows-following position close to the first billows in section A finds large overturns centered at the density interface in section B. Both sections are consistent with the density structure observed in section A. Later drops at the same geographic position, a billows-following position upstream of the billows in section A, find the velocity field changed and no large overturns, indicating the mixing layer no longer exists.

4. Comparison with Laboratory Studies

The initial development of the instability is similar to that found in the laboratory. With the minimum vorticity thickness of 11 m observed in AMP 5852 before the billows appear, the nondimensional wavenumber $\alpha \equiv k(h/2) = (2\pi/70)5.5 = 0.49$. This is somewhat higher than “typical” atmospheric observations of $\alpha \approx 0.4$ [Fritts and Rastogi, 1985]. Our value of α is also quite close to the most unstable mode predicted from linear perturbation theory (0.42–0.49) for error function and hyperbolic tangent profiles [Thorpe, 1971].

The aspect ratio of the billows is 0.14 using a billow amplitude of 10 m. Thorpe [1973] found the aspect ratio to vary with initial gradient Richardson number, from 0.6 for $Ri = 0.05$ to 0.2 for $Ri = 0.15$; thus our observations are consistent with an initial $Ri > 0.15$.

In general, then, the macroscopic character of the billows is similar to laboratory observations and previous atmospheric observations.

Turbulence and mixing generated by the billows are less likely to mimic laboratory flows. Below, we first document the nature of mixing by the instability and confirm the similarity to high-speed shear flows by examining the density structure within the shear layer. We then show that the billows were dissipative as soon as they appeared on the echo sounder, but that shear spectra at dissipation scales take some time to develop a $-5/3$ slope in the inertial subrange.

We also see if the event is well represented as a spatially growing instability. To facilitate a comparison, we use scales common to laboratory studies of shear layers [Koop and Browand, 1979; Dimotakis, 1989]. The comparison leads us to speculate about the importance of an offset of the velocity and density interfaces in determining the magnitude of the dissipation.

4.1. Density Structure

The density structure of the shear layer provides an important clue about mixing within the billows. Heavily averaged profiles smoothly transition between the bounding layers [e.g., Brown and Roshko, 1974], implying that mixing within the shear layer produces a broad range of mixing products, as in gradient diffusion. Instantaneous data collected at scales approaching the Taylor microscale [e.g., Breidenthal, 1981] are very different, finding mixed fluid of only one composition; the averaged profile shape results from averaging in the presence of coherent structures which occur with decreasing frequency away from the centerline. This finding prompted a phenomenological model of mixing in high Re mixing layers [Broadwell and Breidenthal, 1982] which differs markedly from classic gradient dif-

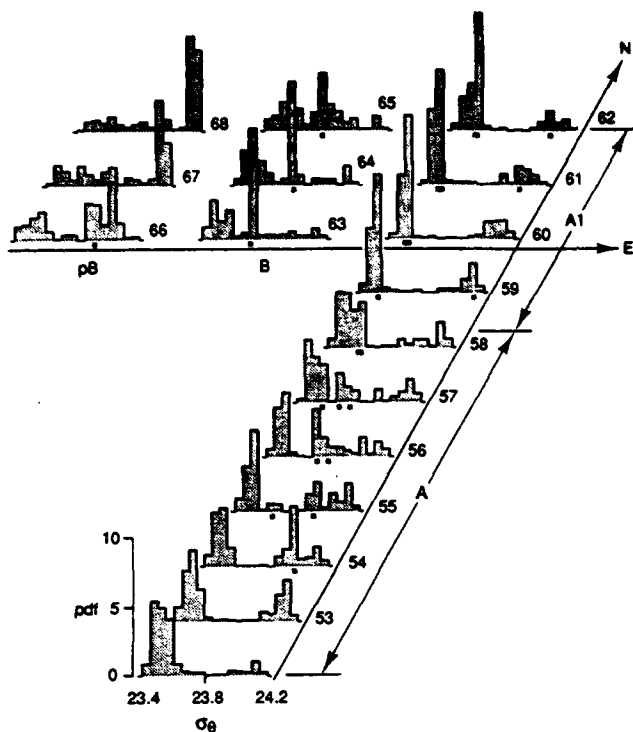


Figure 14. Probability density function (pdf) plots over $23.4 \leq \sigma_\theta < 24.2$ for individual drops, positioned according to geographic location. Solid squares mark the mean density of overturns with $h_{ov} > 2$ m and are seen to correspond to a significant mode in each distribution.

fusion models. We next test which model our data best fit.

The probability density functions (pdf) of the fluid density within $23.4 < \sigma_\theta < 24.2$ for each drop are shown in Figure 14. These isopycnals bound the fluid layer in which the shear instability occurs. They were chosen because they are local minima of L_b and L_{rms} , allowing us to define a fluid layer that should change only owing to internal processes. AMP 5853, collected before large billows were visible on the echo sounder, is a bimodal distribution, with modes at 23.54 and 24.15 kg m^{-3} representing the bounding layers. In AMP 5854, a third mode develops at 23.95 kg m^{-3} , which corresponds to the mean density of the overturn through which AMP passes (computed separately), marked below the pdf with a solid square in Figure 14. For all subsequent drops in sections A, A1, and B, the mean density of the overturns (ρ_{ov}) corresponds to a significant mode in the pdfs which lies between those in AMP 5853, confirming the similarity to high- Re laboratory flows.

Unlike the model of *Broadwell and Breidenthal* [1982], ρ_{ov} changes moving downstream. The overturn mode occurs at progressively lower density in section A, is low in section A1, and then rebounds in section B. This is, however, consistent with our model of the density interface rising with respect to the velocity interface over time at the site where the flow first becomes unstable. This suggests that an offset of the velocity and

density interfaces can greatly affect the composition of the mixed fluid produced in a shear layer. The changing initial conditions permanently impact the development of the shear layer. The resulting vertically homogeneous, horizontally varying density structure has important implications for the final state of the shear layer. We pursue this in the discussion.

4.2. Turbulent Transition

In laboratory flows, the distance downstream of the splitter plate beyond which spatially growing shear layers are turbulent is called the small-scale transition location [*Ho and Huerre*, 1984]. Beyond this point, turbulence is fully developed and molecular-scale mixing proceeds efficiently [*Dimotakis*, 1989]. The establishment of an inertial subrange is a useful criterion for assessing if transition has occurred. In shear flows that are initially laminar, the slopes of shear spectra asymptotically approach $+1/3$ from large negative slopes (e.g., -2). We next form spectra and examine their shape and "universality." Our observations are some of the first to examine transition in a buoyancy-affected shear layer.

Average shear spectra, formed over 10- to 20-m segments from within the billows, approximate the empirical Nasmyth spectrum [*Oakey*, 1982] of the average ϵ over the interval and the theoretically derived spectrum of *Panchev and Kesich* [1969] (Figure 15). (Although the oceanographic community has adopted the Nasmyth spectrum as the spectral form against which to compare measured spectra, several theoretical predictions of the universal spectral form exist. Appendix C presents the theoretical spectrum, a comparison to the Nasmyth spectrum, and that of *Pao* [1965].) All shear spectra from AMP 5854 to 5865 are broadbanded, that is, possess a subrange whose slope is between 0 and $+1/3$ and exhibit viscous rolloffs. We cannot resolve the low-wavenumber portion of the subrange, because vehicle motion contaminates the shear measurements at scales greater than 2 m. Wavenumber spectra normalized by the Kolmogorov velocity and length scales, $(\epsilon\nu^5)^{1/4}$ and $(\epsilon/\nu^3)^{1/4}$, are remarkably similar.

This indicates that a turbulent subrange exists from the time we first observed the billows on the echo sounder, that the billows are dissipative from early in their evolution, and that they are not destroyed by the turbulence. This bears out suspicions voiced by both *Thorpe* [1973] and *Koop and Browend* [1979] that their results on high- Ri flows (greater than 0.15) may not apply to energetic oceanic and atmospheric instabilities. They found the shear layer at large Ri to be a short-lived, inefficient mixing agent which quickly collapsed under gravity.

In our case the instability is highly dissipative and long-lived. Given AMP 5855 and 5864 were collected an hour apart and $N \approx 10^{-2} \text{ rad s}^{-1}$, this mixing event generated strong turbulence for 6 buoyancy periods.

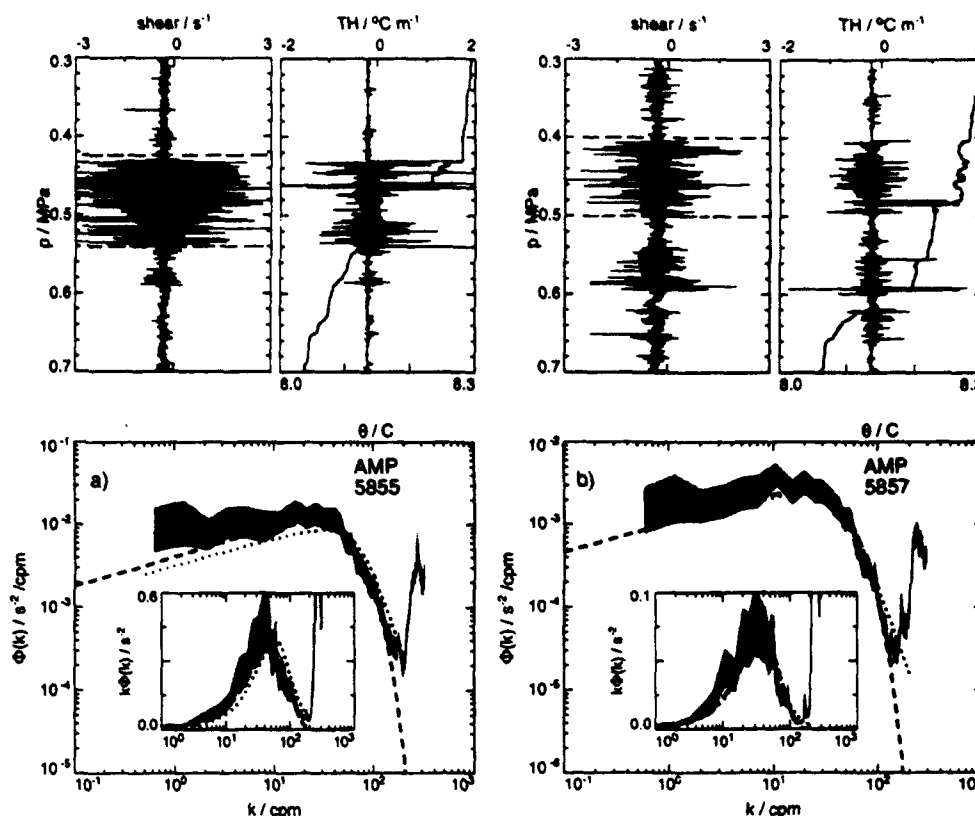


Figure 15. Profiles of small-scale shear, temperature, temperature gradient, and shear and dissipation spectra formed over the depth range marked on the profiles. Dashed lines are Panchev and Kesich spectra for comparison, using ϵ from our standard processing averaged over the same depth and $\nu = 1.43 \times 10^{-6} \text{ m}^2 \text{ s}^{-1}$. Dotted lines are the Nasmyth spectra. (a) Drop 5855: $\tau = 7.7 \times 10^{-6} \text{ W kg}^{-1}$, $Re_b = 1.9 \times 10^4$, and $a = 2$. (b) Drop 5857: $\tau = 1.4 \times 10^{-6} \text{ W kg}^{-1}$, $Re_b = 9.2 \times 10^3$, and $a = 1.6$.

This is 3 times longer than found in low- Re laboratory studies [Thorpe, 1973; Koop and Browand, 1979], even for much lower Ri .

Two departures from the universal spectrum are notable. AMP 5854 and 5855 have spectral slopes of $+1/6$ over 1–10 cpm, slightly steeper than the Nasmyth spectrum (see Figure 15a). This is consistent with the asymptotic approach to a $+1/3$ subrange observed in laboratory flows [Ho and Huerre, 1984] and suggests the turbulence has not yet achieved an equilibrium state. These spectra also roll off at lower wavenumbers than the predicted spectra; for the Panchev and Kesich spectrum, a Kolmogorov constant of 2 rather than the typical value of 1.6 provides a better fit to the measured spectra. The other oddity is less easily understood. Our spectra systematically peak at wavenumbers half the peak in the Nasmyth spectrum; that is, if the Nasmyth spectrum is given by $\Phi_N(\epsilon, \nu)$, our data are better fit with $2\Phi_N(\epsilon/2, \nu)$. As shown in Appendix C, the Panchev and Kesich spectrum peaks at a lower wavenumber than the Nasmyth spectrum. We have independently confirmed that our data collection and analysis software correctly reproduces an electroni-

cally generated white noise signal, and that line spectra are properly measured.

In AMP 5853 dissipation rates are high in and below the density step at 0.45 MPa, before large overturns form (Figure 7a) and where $Ri_{12} < 0.25$. Spectra from this drop are broadbanded, but the rolloff is not well fit by the theoretical spectra. This is in marked contrast to low- Re laboratory experiments in which turbulence was observed only after the billows attained maximum amplitude [Thorpe, 1973; Koop and Browand, 1979]. However, this is in good agreement with atmospheric observations, in particular those of Browning [1971]. He observed 17 "billow" events with radar, all of which were preceded by a turbulent scattering layer. Indeed, radar requires the presence of small-scale turbulence to image the larger-scale instability [Gage, 1989].

There are several possible reasons for the discrepancy between the laboratory observations and our data. In addition to the large difference in Re , an effort is often made in laboratory studies to keep the upstream flow laminar, whereas in the tidal channel, the flow can seldom be considered laminar. We cannot isolate a particular aspect of the flow that gives rise to the discrepancy,

but note that transition in some geophysical flows may be qualitatively different from transition in ideal laboratory settings.

4.3. Spatial Evolution

To find a simple description of the evolution of the instability, we compare our data with a spatially growing shear layer. Because the shear layer is already unstable by AMP 5853, we assume an origin upstream of it, at AMP 5852. We normalize the downstream distance and layer thickness by the initial vorticity thickness, $h = 11$ m. To quantify the dissipation in the shear layer, we average ϵ over L_ϵ , roughly the distance over which $\epsilon > 10^{-7} \text{ W kg}^{-1}$ where S_{12}^2 is large. The elevated ϵ layer is consistently bounded by several meters of fluid in which ϵ is well below the threshold.

The growth rate, h/x , is roughly constant at $O(0.005)$ (dotted line in Figure 16a), suggesting the shear layer is slowly but steadily growing. This growth rate is a tenth

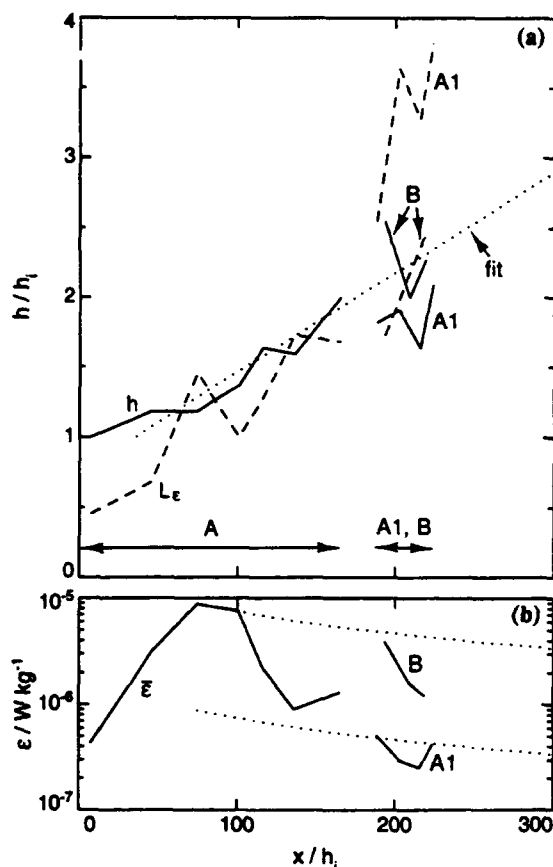


Figure 16. Growth curves assuming a spatially growing instability. The origin is taken to be AMP 5852, where $h_i \approx 11$ m. (a) The h , L_ϵ (dashed line), and a linear fit (dotted line). The trend in L_ϵ is similar to that for h but less consistent, as expected for an unaveraged measurement. (b) The $\bar{\epsilon}$ and similarity prediction (dotted line), using $\bar{\epsilon}_0 = 8.8 \times 10^{-6} \text{ W kg}^{-1}$ and $\bar{\epsilon}_0 = 8.8 \times 10^{-7} \text{ W kg}^{-1}$ for the growth rate marked in Figure 16a.

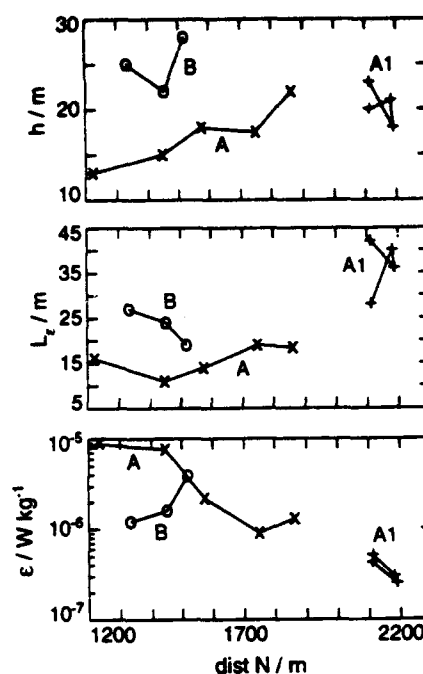


Figure 17. Outer scales as a function of distance north in the billows-following frame (cf. Figure 4). Different symbols are used for each section: crosses for section A, pluses for section A1, and open circles for section B.

that of unstratified flows in the laboratory [Dimotakis, 1989] but similar to growth curves of stratified shear layers for $Ri > 0.1$ [Thorpe, 1973; Koop and Browand, 1979]. Changes in the mean velocity field are consistent with spatial growth at fairly large initial Ri .

Changes in the dissipation rate are not consistent with a spatially growing shear layer. In a self-similar shear layer, the dissipation rate is expected to be inversely proportional to h , such that $\int_0^h \epsilon dz = \text{constant}$. The doubling of h between AMP 5854 and 5858 should cause $\bar{\epsilon}$ to decrease by a factor of 2. After peaking at $\bar{\epsilon} \approx 8.8 \times 10^{-6} \text{ W kg}^{-1}$, the observed downstream decrease significantly exceeds that expected for a self-similar flow, shown by the dotted lines in Figure 16b. The mean dissipation rate near $x/h_i = 200$ changes dramatically between sections A1 and B; obviously spatial growth alone cannot explain the observations.

As already mentioned, the shear layer was not steady, and it suggests a reference frame moving with the billows would be more appropriate to assess the evolution. Replotting $\bar{\epsilon}$ versus distance in the billows-following frame (Figure 4c) finds it regularly decreasing northward (Figure 17). Changes in turbulence levels along section A appear largely related to the changes in position within the set of billows. This suggests the changes in $\bar{\epsilon}$ are due to the change in offset of the velocity and density interfaces along the set.

In the billows-following frame, AMP 5863 resamples the shear layer between AMP 5855 and 5856. For these drops the change in $\bar{\epsilon}$ agrees with predictions for a self-

Similar flow (Figure 16b), that is, both points lie along the predicted curve. That changes in $\bar{\tau}$ of fluid tracked in a billows-following frame are consistent with spatial growth lends support to our suggestion that differences in $\bar{\tau}$ along the set arise from differing initial conditions rather than varying degrees of temporal decay.

To crudely estimate the impact of interface offset on the dissipation rate, we assume all billows have the same rate of downstream decrease in $\bar{\tau}$ (parallel dotted lines in Figure 16b). If the origin is the same for all the billows, the initial value of $\bar{\tau}$ must have varied by slightly more than a factor of 10. All other initial conditions being the same, which of course is a big assumption, the interface offset may lead to 1 order of magnitude variation in the maximum value of $\bar{\tau}$.

5. Overturns Within the Shear Layer

We briefly characterize turbulence within the shear layer using scales and parameters common to oceanographic studies. We follow Wijesekera *et al.* [1993] and H. Peters *et al.* (The mechanisms of equatorial turbulent mixing, 2, Detail and scaling of mixing events, submitted to the *Journal of Geophysical Research*, 1993) by conditionally sampling only overturns. Within the overturns, values are averaged before forming the various scales, the idea being that turbulent length scales are properly defined only within the unstable portions of the water column.

Every AMP drop collected after the billows form shows large overturns, $h_{ov} > 5$ m. Of our 12 profiles, none sample a stable, high-gradient region. Either the profiler never passed through braids, or the braids in this realization are also sites of overturning. Given the large initial Re , secondary Kelvin-Helmholtz instabilities are anticipated [Corcos and Sherman, 1976], as are streamwise vortices [Breidenthal, 1981]. Evidence for secondary K-H instability can be seen in Plate 1, where a small billow is imbedded in the scattering layer just upstream of the AMP 5854 trajectory.

We form average properties for all overturns greater than 2 m; smaller overturns contain too few data points to form stable estimates. Considering the largest over-

turns in each profile, only ϵ_{ov} and N_{ov}^2 display monotonic changes in the billows-following reference frame. Both are smallest to the north (section A1); the trend in ϵ_{ov} mimics that of $\bar{\tau}$ from the previous section. Low N_{ov}^2 in section A1 probably reflects that most of the overturns occur in weakly stratified fluid.

Table 2 presents the mean and range of properties of all the overturns in the shear layer. For all the observed overturns, $Re_b > 2000$, easily satisfying the criterion of Gargett *et al.* [1984] for isotropy at dissipation scales. The large variations in ρ_{ov} reflect changes in the vertical offset of the density and velocity interfaces over the set of billows. With the exception of the largest overturn in drop 5861, $\epsilon > 10^{-7}$ W kg⁻¹. The smaller overturns are quite energetic and for AMP 5858 and 5861 are associated with higher ϵ_{ov} than the larger overturns. The mean overturn size within the shear layer is 7.1 m with $\overline{L_{rms}} = 2.58$ and $\overline{L_b} = 2.71$. The ratio $\overline{L_{rms}}/\overline{L_b} = 0.95$ is close to 1, as has been observed in almost all previous oceanic thermocline studies [e.g., Dillon, 1982; Peters *et al.*, 1988].

The equivalence of L_b and L_{rms} is often taken to indicate that stratification has limited the maximum scale of overturning [e.g., Rohr *et al.*, 1988], a state that Ivey and Imberger [1991] find to be maximally efficient at mixing. Using the largest overturns in each profile, we find no regular trend in $L_b/L_{rms} \approx 1$ with time or in the billows-following frame, although $L_{rms} > L_b$ in section A, while $L_b > L_{rms}$ in section B. A plot of L_{rms} versus L_b reveals wide scatter (Figure 18), $0.5 < L_b/L_{rms} < 4.3$. For $h_{ov} \leq 5$ m, L_b tends to exceed L_{rms} ; for $h_{ov} > 5$ m, the reverse is true.

The data allow estimation of the mixing efficiency, $\gamma \equiv \chi_{pe}/\epsilon_{ov}$, where χ_{pe} is the dissipation rate of potential energy. Because χ_{pe} cannot as yet be measured in a salt-stratified fluid, we estimate it from χ , assuming that the dissipation rates of heat and salt are in proportion to their respective contributions to the mean density gradient. Following Gregg [1987], we use

$$\chi_{pe} \equiv [g\alpha/N]^2(1 + 1/R_\rho^2)\chi \quad [\text{W kg}^{-1}] \quad (4)$$

where α is the thermal expansion coefficient, $R_\rho \equiv \alpha(\partial T/\partial z)/\beta(\partial S/\partial z) \approx -0.05$ is the stability ratio, T

Table 2. Average Properties of the 25 Overturns with $h_{ov} > 2$ m

Variable	Mean	Range
h_{ov} , m	7.1	2-19
ρ_{ov} , kg m ⁻³	23.7	23.5-24.13
L_{rms} , m	2.58	0.43-7.45
L_b , m	2.71	0.54-8.7
ϵ_{ov} , W kg ⁻¹	1.83×10^{-6}	5.9×10^{-8} - 8.4×10^{-6}
N^2 , s ⁻²	6.7×10^{-5}	4.8×10^{-6} - 3.1×10^{-4}
Re_b , negative	3.0×10^4	2.2×10^3 - 1.5×10^5
χ_{ov} , K ² s ⁻¹	1.4×10^{-7}	2.3×10^{-10} - 1.2×10^{-6}
χ_{pe} , W kg ⁻¹	9.8×10^{-7}	3.7×10^{-9} - 6.2×10^{-6}
γ , negative	0.58	0.17-1.3

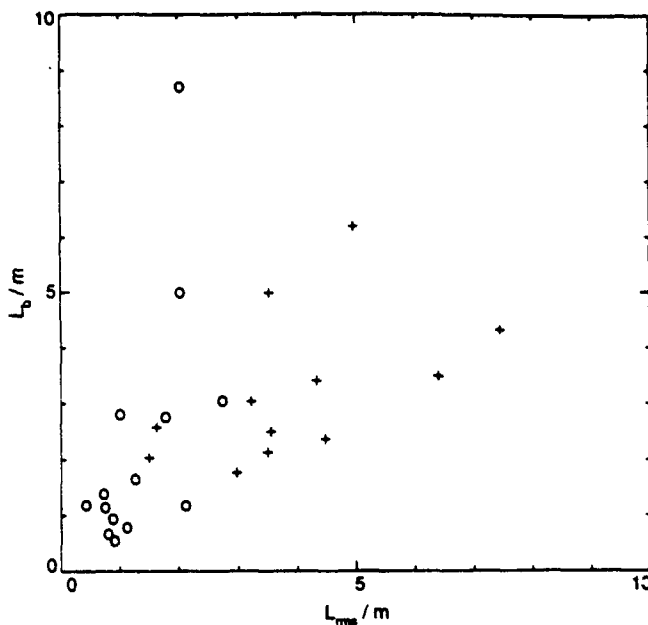


Figure 18. Scatter plot of L_{rms} versus L_b for overturns greater than 2 m within the mixing layer. Overturns greater than 5 m are marked by crosses, those with $h_{ov} < 5$ m are marked by o's. A least squares fit yields $L_b = 0.86 L_{rms}$, with a correlation coefficient of 0.47, or Kendall's τ of 0.49.

is temperature, S is salinity, and β is the haline contraction coefficient. For the largest overturns, $0.17 < \gamma \leq 1.3$, with an average of 0.58, which is larger than previous estimates of γ based on simultaneous ϵ and χ measurements (0.24 [Oakey, 1982]; 0.12 [Peters and Gregg, 1988]; and $0.12 < \gamma < 0.48$ [Moum et al., 1989]). Averaged over sections, γ is greatest in section A (0.72), least in A1 (0.35), and intermediate in B (0.65). This suggests that offset of the interfaces also affects γ , but uncertainties in χ_{pe} are larger than the differences.

6. Summary and Discussion

6.1. Summary

We made two passes through a kilometer-long set of 20-m-tall billows within an unstable shear layer over a time period of 1 hour. Continuous velocity profiles indicate a rapid increase in shear passing by Bush Point. Initial conditions of the mixing event are (1) $\Delta U/2\bar{U} \approx 0.5$, $\Delta\rho/\rho_0 \approx 5 \times 10^{-4}$ across the high-gradient region in a continuously salt-stratified (large Schmidt number) flow. The initial vorticity thickness is $h_i \approx 11$ m. (2) $Ri < 0.25$ just beneath the large density gradient before the echo sounder reveals billows. (3) $Re \approx 3 \times 10^6$. The wavenumber and aspect ratio of the billows which form are consistent with the initial observed h and Ri . Within the mixing layer, several more points can be made.

1. Instantaneous density profiles through the billows reveal large-scale overturning, and we find these

overturns, in all cases, to be associated with elevated dissipation rates. In the billows-following frame, the overturns occur in progressively less dense fluid to the north. This implies changes in the offset of the velocity and density interfaces over time where the billows first form.

2. The instantaneous distribution of density is consistent with mixing models of turbulent shear layers at large Re [Broadwell and Breidenthal, 1982]. The persistence of overturn modes throughout the mixing event, long after the initial formation of the billow and despite an obvious longitudinal structure in the density field, supports the notion that billows permanently retain characteristics imparted at their formation, even in a continuously stratified fluid.

3. The transition to turbulence, its persistence, and the mixing efficiency of billows in geophysical flows can be qualitatively different than in the laboratory. The billows are strongly turbulent over the entire sampling period, even in their early development. Turbulence within the shear layer is long-lived in comparison to low- Re laboratory experiments which find the shear layer to be relaminarized within two buoyancy periods [Thorpe, 1973; Koop, 1976]. Our observations indicate that strong dissipation persists for more than six buoyancy periods.

4. Although h increases regularly over sections A–B, like a spatially growing stratified shear layer, $\bar{\epsilon}$ decreases more rapidly than $1/h$ in section A and in section A1 is much less than expected. Values of $\bar{\epsilon}$ from section B, which resample part of section A, roughly follow values predicted for a self-similar shear layer. We conclude that spatial growth adequately represents the outer scale variations but that changes in interface offset strongly affect the level of dissipation.

5. The energy scales L_b and L_{rms} display no significant trends in geographic coordinates or a billows-following reference frame. Their ratio remains within a factor of 2 of unity for the largest overturns and averages 0.95. Turbulent activity of overturns remains strong over the entire sampling period, $Re_b > 2000$, and large billows may be quite efficient mixers, $\gamma \approx 0.6$.

6.2. Discussion

Previous studies of buoyancy-affected shear layers [Thorpe, 1973; Koop and Browand, 1979] have emphasized the importance of Ri in determining the character of a shear instability. This study indicates the importance of Re and interface offset. As noted by Koop and Browand, the parameter space to be explored is indeed large.

Observations by Browning [1971] suggest interface offset is a common feature. In most of the 17 atmospheric billow events he observed, the interfaces were offset; eight billows occurred "on the edge of a stability maximum" and four occurred in uniform stratification, although all were observed at a level of maximum shear.

Together with our data, this implies that displaced velocity and density interfaces at kilometer scales (the size of the mixing patch) are the rule rather than the exception in geophysical fluids.

The long-lived nature of active turbulence in this study implies a fundamental difference between this natural shear layer and those at low Re in the laboratory. Energetic, naturally occurring instabilities, which transition to turbulent motion soon after their formation, will necessarily be more effective at producing mixed fluid, especially if they are longer lived than their small counterparts. The mixing efficiency of big billows may be substantially greater than that of small billows. There is mounting evidence that mixing rates are very small in the bulk of the ocean thermocline. Our study implies that the importance of sites of vigorous mixing may be underestimated if only their scale is considered; they may also be more efficient at producing mixed fluid.

The first-order variability in dissipation rate of the shear layer is captured in the billows-following reference frame. However, the change in turbulence levels between sections A and AMP 5864 and 5865 is significant and suggests the turbulence is beginning to decay. If this is the case, then some of the trend in ϵ with layer density may be due to different sampling times. In the billows-following frame, we first sampled the southern portion, when these billows were first forming. We sampled the northern part well after they formed. If the billows did not behave in a self-similar fashion, we have misinterpreted the data.

We did not track the mixing event long enough to observe the final state of the mean fields. In this study, all but the last profile through the shear layer reveal a large mixed layer bounded by high-gradient regions, similar to the model of Woods and Wiley [1972]. However, two points cloud this finding. First, in AMP 5865 the density field appears to be relaxing to a single, thick high-gradient layer. It is possible that up to this point, coherent structures dominate the density structure, but that after they are dissipated, unmixed fluid invades the billow structures and the density field relaxes to a smoothly varying, stable state. Second, even if a mixed layer persists after the billows dissipate, the longitudinal density structure in the shear layer will generate a circulation that will tend to restratify the shear layer. A vertical, homogeneous, horizontally stratified layer will generate a lock-exchange type of flow, tending to produce a smoothly varying vertical density gradient. Further observations are required to resolve this issue.

If we estimate ϵ as q^3/l , taking $q \approx 0.1\Delta U$ and $l = 20$ m, and use the mean stratification $N^2 = 10^{-4} \text{ s}^{-2}$, we find $Re_b = 4.5 \times 10^4$, close to the mean value of the largest overturns. Apparently simple scaling arguments provide good order-of-magnitude estimates of the turbulent activity of the mixing event regardless of the interface offset.

Unanswered is a quantification of the importance of turbulence in an energy balance of the mixing event. In particular, we can assess the importance of dissipation in changing the shear and how much of the change in potential energy is due to the buoyancy flux. The energy fluxes into and out of the shear layer provide clues about the generation mechanism of the instability and a measure of energy loss due to internal wave radiation. These topics are pursued by Seim and Gregg (1993).

Appendix A: Barotropic Velocities

Owing to poor navigation data, we are unable to form absolute velocities with the ADCP data. We estimate the flow speed during the time we were sampling with a linked tidal transport model of Puget Sound developed by Lavelle *et al.* [1988]. Using finite difference techniques, they solve a set of linearized momentum and continuity equations in one dimension, constrained to be the best fit to observed water level data. The model predicts the amplitude and phase of the principal tidal components at over 50 calibration points to within ± 2 cm and $\pm 5^\circ$. The model also predicts the average velocity at 589 cross sections throughout the Sound. While this should be an equally accurate estimate of the sectionally averaged velocity, the few sections that have been well instrumented display large vertical and horizontal gradients in velocity at tidal frequencies. The model velocities are therefore of limited accuracy at a given lateral position. Interestingly, Bush Point is one of the few sections that has been instrumented. Three moorings, each with multiple current meters, were maintained across Bush Point for several months in 1977. In cotidal charts of the velocity, the shear at Bush Point is principally in the vertical [Lavelle *et al.*, 1988]. The secondary lateral structure displays a velocity core centered in the east half of the channel.

We estimate the current speed at our AMP drop locations by first predicting the tidal current at all model points between the sections that bound the area we sampled (Figure A1). We then interpolate between the curves using our time and position information. Only in section A is the interpolated curve much different than the individual curves. For this section the flow rapidly accelerates as it moves through the lateral constriction. Using data collected on anchor just north of Bush Point in May 1988 with the same instrument system, we find the model underpredicts the speed by 20%.

Appendix B: Dissipation Rate Errors

Assessing the uncertainty associated with dissipation rate estimates is not straightforward. Because of the highly skewed nature of the distribution of ϵ , standard statistical procedures that assume normal distributions cannot be applied. Briefly, we consider two forms of

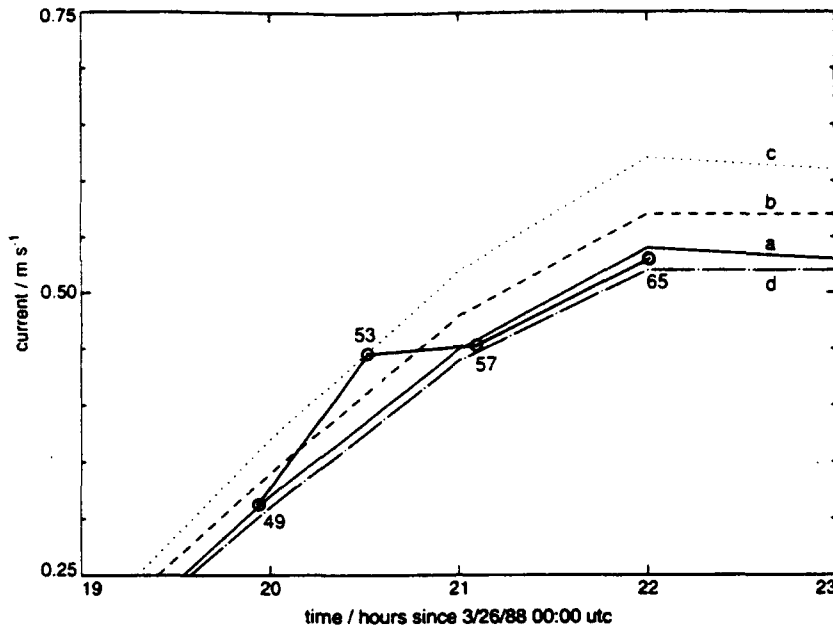


Figure A1. Predicted tidal currents at the appropriate model sections, labeled a–d, moving from south to north through Bush Point. The solid line is the interpolated current along the ship track, with AMP drop numbers marked.

error in our estimates: a bias in absolute estimates due to calibration and processing errors and a random error due to natural variability of the dissipation which controls the precision of our estimates. We are less concerned with the former in this study, because the two shear probes in AMP were not changed during the course of the experiment and thus a calibration error affects all data equally. As stated in the text, we believe we are within a factor of 2 of the actual dissipation rate.

Of more concern is to realistically bound estimates developed for each AMP profile to determine whether the trends we observe are statistically significant. This may be approached in a number of ways. From theory, we anticipate that ϵ is lognormally distributed in statistically homogeneous, isotropic turbulence [e.g., Gurvich and Yaglom, 1967]. Confidence limits for lognormally distributed data are a function of the number of samples and the standard deviation of the natural logarithm of the ϵ estimates, $\sigma_{\ln \epsilon}$ [Land, 1975]. Using the 0.5-m estimates from within the elevated ϵ region of the shear layer (L_ϵ), we find $\sigma_{\ln \epsilon} < 1.5$. Over 20 m we obtain eighty 0.5-m estimates by overlapping data windows 50%, which suggests the confidence limits are somewhat less than a factor of 2. The validity of this approach is questionable, since many of the distributions depart from lognormality and the individual estimates are certainly not independent (i.e., uncorrelated). In a practical sense, the ϵ estimates are based on summing a large number of spectral estimates, each of which is a sum of squares, and hence are χ_n^2 distributed with n degrees of freedom. If we are grossly conservative and assume each 0.5-m estimate has 2 degrees of freedom, a

20-m average has 80 degrees of freedom, or confidence limits of about 20%. The precision of our estimates likely lies somewhere between these sets of limits.

Appendix C: Shear Spectra at Dissipation Scales

Several theoretical predictions of the universal spectral form exist. Pao [1965] presents a simple model of the spectrum, based on the assumption that the transfer of energy across a given wavenumber k in the inertial subrange is equal to the dissipation rate at viscous scales. Although his model adequately represents the initial roll-off of the velocity spectrum at small scales, measured spectra at Kolmogorov scales roll off more rapidly than Pao's model predicts. Saffman [1963] derives a form of the spectrum, for $k > k_s$, where $k_s \equiv (\epsilon/\nu^3)^{1/4}$ is the Kolmogorov wavenumber, which rolls off more rapidly than Pao's model predicts. Panchev and Kesich [1969], noting that the assumptions underlying Pao's model cannot hold as the peak of the shear spectrum is approached, propose an "interpolation form" which joins Pao's spectrum at low wavenumbers to Saffman's spectrum at high wavenumbers. In nondimensional form, the three-dimensional spectrum is

$$\frac{E(k)}{(\epsilon \nu^5)^{1/4}} = \left(a \left(\frac{k}{k_s} \right)^{-5/3} + \sqrt{\frac{3}{2}} a^{3/2} \left(\frac{k}{k_s} \right)^{-1} \right) \exp \left(-\frac{3}{2} a \left(\frac{k}{k_s} \right)^{4/3} - \sqrt{\frac{3}{2}} a^{3/2} \left(\frac{k}{k_s} \right)^2 \right) \quad (C1)$$

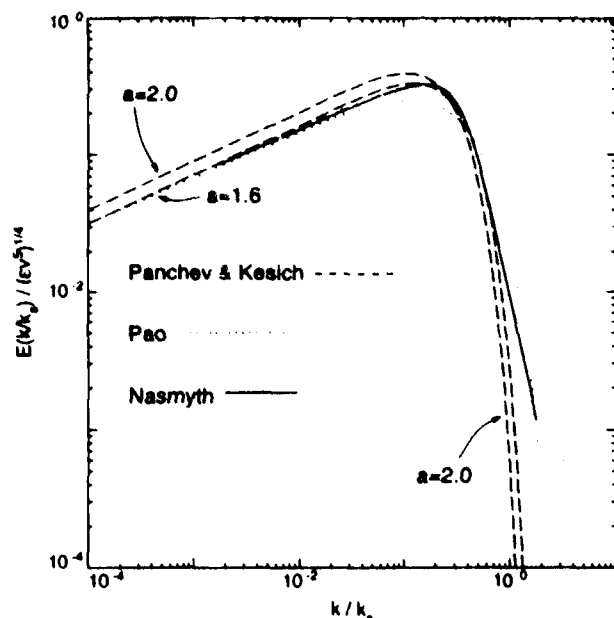


Figure C1. Comparison of the Pao, Nasmyth, and Panchev and Kesich high-wavenumber shear spectra. The Panchev and Kesich spectrum is plotted with two values of the Kolmogorov constant, $a = 1.6$ and 2.0 .

where a is the Kolmogorov constant and ν is the kinematic viscosity. To compare this with our shear probe measurements, we convert to the one-dimensional transverse velocity form using

$$\frac{E_1(\bar{k}_1)}{(\epsilon\nu^5)^{1/4}} = \frac{1}{2} \int_{\bar{k}_1}^{\infty} \left(1 + \frac{\bar{k}_1^2}{\bar{k}^2}\right) \frac{E(\bar{k})}{\bar{k}} d\bar{k}$$

which, upon a change of variables to $\zeta = \bar{k}_1/\bar{k}$ where $\bar{k} = k/k_s$ and \bar{k}_1 denotes a component of the wavevector, yields

$$\frac{E_1(\bar{k}_1)}{(\epsilon\nu^5)^{1/4}} = \frac{\bar{k}_1^{-5/3}}{2} \int_0^1 (1 + \zeta^2) \left(a\zeta^{2/3} + \sqrt{\frac{3}{2}} a^{3/2} \bar{k}_1^{2/3} \right) \exp \left(-\frac{3}{2} a \left(\frac{\bar{k}_1}{\zeta} \right)^{4/3} - \sqrt{\frac{3}{2}} a^{3/2} \left(\frac{\bar{k}_1}{\zeta} \right)^2 \right) d\zeta. \quad (C2)$$

Plotted in Figure C1 are the Pao, Nasmyth, and Panchev and Kesich spectra, with $a = 1.6$ for the two theoretical spectra. Although all three asymptotically approach the same curve at low wavenumbers, their behavior near the peak of the shear spectrum and in the roll-off differs markedly. The Pao spectrum rolls off most gently, whereas the Nasmyth spectrum is the most peaked. The shape of the high wavenumber roll-off is similar for the two theoretical spectra; the Nasmyth spectrum is almost linear on the log-log plot, like a power law.

Spectra from the first billows sampled are better fit by the Panchev and Kesich spectrum with $a = 2$. The effect of changing this constant is illustrated in Figure C1;

the spectral level in the inertial subrange is increased, and the wavenumber where the spectrum begins to roll off is decreased.

Acknowledgments. Washington State Sea Grant funded collection of these data, and the Office of Naval Research University Research Initiative "Mixing to Mesoscale" funded the bulk of the analysis. This paper benefitted greatly from discussions with Jim Riley, Eric D'Asaro, Kraig Winters, and Dave Winkel. We also thank the AMP Group—in particular Jack Miller, Dale Hirt, Steve Bayer, and Donna Sorensen—for collecting the data, and Bob Miyamoto for development of the acoustic system. This is contribution 1984 from the University of Washington School of Oceanography.

References

- Armi, L., Hydraulics of two flowing layers with different densities, *J. Fluid Mech.*, **163**, 27–58, 1986.
- Breidenthal, R., Structure in turbulent mixing layers and wakes using a chemical reaction, *J. Fluid Mech.*, **109**, 1–24, 1981.
- Broadwell, J. E., and R. E. Breidenthal, A simple model of mixing and chemical reaction in a turbulent shear layer, *J. Fluid Mech.*, **125**, 397–410, 1982.
- Brown, G. L., and A. Roshko, On density effects and large structures in turbulent mixing layers, *J. Fluid Mech.*, **64**(4), 775–816, 1974.
- Browning, K. A., Structure of the atmosphere in the vicinity of large-amplitude Kelvin-Helmholtz billows, *Q. J. R. Meteorol. Soc.*, **97**, 283–299, 1971.
- Corcos, G.M., and F.S. Sherman, Vorticity concentration and the dynamics of unstable free shear layers, *J. Fluid Mech.*, **73**, 241–264, 1976.
- Dillon, T.M., Vertical overturns: A comparison of Thorpe and Ozmidov scales, *J. Geophys. Res.*, **85**, 1910–1916, 1982.
- Dimotakis, P. E., Turbulent free shear layer mixing, paper presented at the A. Inst. of Aeronaut. and Astronaut. 27th Aerospace Sciences Meeting, Reno, Nev., Jan. 9–12, 1989.
- Fritts, D. C., Shear excitation of atmospheric gravity waves, II, Nonlinear radiation from a free shear layer, *J. Atmos. Sci.*, **41**(4), 524–537, 1984.
- Fritts, D. C., and P. K. Rastogi, Convective and dynamical instabilities due to gravity wave motions in the lower and middle atmosphere: Theory and observations, *Radio Sci.*, **20**(6), 1247–1277, 1985.
- Gage, K. S., Radar observations of the free atmosphere: Structure and dynamics, in *Radar in Meteorology*, pp. 159–175, American Meteorological Society, New York, 1989.
- Gargett, A. E., T. R. Osborn, and P. W. Nasmyth, Local isotropy and the decay of turbulence in a stratified fluid, *J. Fluid Mech.*, **144**, 231–280, 1984.
- Geyer, W. R., Time-dependent, two-layer flow over a sill, in *The Physical Oceanography of Sea Straits*, edited by L. J. Pratt, pp. 421–432, Kluwer Academic, Norwell, Mass., 1990.
- Geyer, W. R., and J. D. Smith, Shear instability in a highly stratified estuary, *J. Phys. Oceanogr.*, **17**, 1668–1679, 1987.

- Gregg, M. C., Diapycnal mixing in the thermocline: A review, *J. Geophys. Res.*, **92**, 5249–5286, 1987.
- Gurvich, A. S., and A. M. Yaglom, Breakdown of eddies and probability distributions for small-scale turbulence, *Phys. Fluids*, **10** suppl., 59–65, 1967.
- Ho, C., and P. Huerre, Perturbed free shear layers, *Annu. Rev. Fluid Mech.*, **16**, 365–424, 1984.
- Ivey, G. N., and J. Imberger, On the nature of turbulence in a stratified fluid, I, The energetics of mixing, *J. Phys. Oceanogr.*, **21**, 650–658, 1991.
- Koop, C. G., Instability and turbulence in a stratified shear layer, Ph.D. dissertation, 245 pp., Univ. of South. Calif., Los Angeles, 1976.
- Koop, C. G., and F. K. Browand, Instability and turbulence in a stratified fluid with shear, *J. Fluid Mech.*, **93**, 135–159, 1979.
- Land, C. E., Tables of confidence limits for linear functions of the normal mean and variance, in *Selected Tables in Mathematical Statistics*, III, edited by H. L. Harter and D. B. Owen, pp. 385–419, American Mathematical Society, Providence, R. I., 1975.
- Lavelle, J. W., H. O. Mofjeld, E. Lempriere-Doggett, G. A. Cannon, D. J. Pashinski, E. D. Cokelet, L. Lytle, and S. Gill, A multiply-connected channel model of tides and tidal currents in Puget Sound, Washington, and a comparison with updated observations, *NOAA Tech. Mem., ERL PMEL-84*, 1–24, 1988.
- Lawrence, G. A., F. K. Browand, and L. G. Redekopp, The stability of a sheared density interface, *Phys. Fluids A*, **3**, 2360–2370, 1991.
- Miles, J. W., On the stability of heterogeneous shear flows, *J. Fluid Mech.*, **10**, 496–508, 1961.
- Moum, J. N., D. R. Caldwell, and C. A. Paulson, Mixing in the equatorial surface layer, *J. Geophys. Res.*, **94**, 2005–2021, 1989.
- Oakey, N. S., Determination of the rate of dissipation of turbulent energy from simultaneous temperature and shear microstructure measurements, *J. Phys. Oceanogr.*, **12**, 256–271, 1982.
- Panchev, S., and D. Kesich, Energy spectrum of isotropic turbulence at large wavenumbers, *C. R. Acad. Bulg. Sci.*, **22**, 627–630, 1969.
- Pao, Y., Structure of turbulent velocity and scalar fields at large wavenumbers, *Phys. Fluids*, **8**, 1063–1075, 1965.
- Peters, H., and M. C. Gregg, Some dynamical and statistical properties of equatorial turbulence, in *Small-Scale Turbulence and Mixing in the Ocean*, edited by J. C. J. Nihoul and B. M. Jamart, pp. 185–200, Elsevier, New York, 1988.
- Peters, H., M. C. Gregg, and J. M. Toole, On the parameterization of equatorial turbulence, *J. Geophys. Res.*, **93**, 1199–1218, 1988.
- Rohr, J. J., E. C. Itsweire, K. N. Helland, and C. W. Van Atta, Growth and decay of turbulence in a stably stratified shear flow, *J. Fluid Mech.*, **195**, 77–111, 1988.
- Saffman, P. G., On the fine-scale structure of vector fields convected by a turbulent fluid, *J. Fluid Mech.*, **16**, 545–572, 1963.
- Thorpe, S. A., Experiments on the instability of stratified shear flows: Miscible fluids, *J. Fluid Mech.*, **46**, 299–319, 1971.
- Thorpe, S. A., Experiments on instability and turbulence in a stratified shear flow, *J. Fluid Mech.*, **61**, 731–751, 1973.
- Thorpe, S. A., Turbulence and mixing in a Scottish loch, *Phil. Trans. R. Soc. London A*, **286**, 125–181, 1977.
- Thorpe, S. A., Transitional phenomena and the development of turbulence in stratified fluids: A review, *J. Geophys. Res.*, **92**, 5231–5248, 1987.
- Wesson, J., and M. C. Gregg, Mixing at Camarinal Sill in the Strait of Gibraltar, *J. Geophys. Res.*, in press, 1994.
- Wijesekera, H. W., T. M. Dillon, and L. Padman, Some statistical and dynamical properties of turbulence in the oceanic pycnocline, *J. Geophys. Res.*, **98**, 22,665–22,679, 1993.
- Woods, J. D., and R. L. Wiley, Billow turbulence and ocean microstructure, *Deep Sea Res.*, **19**, 87–121, 1972.

M. C. Gregg and H. E. Seim, Applied Physics Laboratory, College of Ocean and Fishery Sciences, University of Washington, 1013 N.E 40th Street, Seattle, WA 98105.

(Received August 12, 1993; revised December 21, 1993; accepted December 28, 1993.)